



Supplementary Materials for

A massive helium star with a sufficiently strong magnetic field to form a magnetar

Tomer Shenar *et al.*

Corresponding author: Tomer Shenar, T.Shenar@uva.nl

Science **381**, 761 (2023)
DOI: 10.1126/science.ade3293

The PDF file includes:

Materials and Methods
Supplementary Text
Figs. S1 to S11
Tables S1 and S2
References

Other Supplementary Material for this manuscript includes the following:

Data S1

Materials and methods

Observational data

We acquired spectropolarimetric observations (Stokes I and V) of HD 45166 on 2022 February 17 and 19 with the ESPaDOnS spectropolarimeter (53) mounted on the CFHT (program ID 22AC08; PI: Shenar). A total of eight 1-hr exposures (four per night), each divided into four sub-exposures, resulted in typical signal-to-noise (S/N) of $\approx 150 - 200$ per wavelength bin at $\approx 5000 \text{ \AA}$ and a resolving power $R = 65\,000$. The spectra cover the wavelength range $3668 - 10\,480 \text{ \AA}$. The data were reduced and wavelength-calibrated using CFHT’s standard UPENA pipeline (54). Including the subexposures, a total of 32 Stokes I and V ESPaDOnS spectra were obtained. The co-added ESPaDOnS I and V spectra are shown in Fig. 2.

Additionally, we measured RVs from archival optical spectra obtained with three additional spectrographs. The first set of archival data was acquired between 1998 to 2004 using the Coudé spectrograph at the 1.6 m telescope of the LNA in Itajubá, Brazil (55), and has been previously described by (16). The majority of LNA spectra cover a modest spectral range ($4520 - 4960 \text{ \AA}$) at a resolving power of $R \approx 7000$, reaching a typical S/N of $20 - 30$ in the continuum. A few additional higher-resolution spectra ($R \approx 20\,000$) covering the range $3830 - 4580 \text{ \AA}$ were also used. In total, 103 LNA spectra were available.

The second set of archival spectroscopic data were obtained in 2002 with the FEROS instrument (56) mounted at the 1.52 m telescope of the European Southern Observatory (ESO) in La Silla, Chile (56). These data cover a spectral range $3830 - 9215 \text{ \AA}$ at a resolving power of $R = 48\,000$, with typical S/N of 80 in the range $4500 - 7000 \text{ \AA}$ decreasing down to ≈ 35 at the blue and red edges. A total of 36 FEROS spectra are available, taken at a high cadence over a few nights. The data reduction and calibration were also described previously (16).

The third and final archival spectroscopic dataset was acquired in 2019 – 2021, with the

exception of a single spectrum in 2012, using the HERMES spectrograph (57) mounted on the 1.2 m Mercator telescope at the Observatorio del Roque de Los Muchachos on La Palma, Spain (57). HERMES spectra cover the wavelength range from 3770 to 9000 Å with a spectral resolving power of $R \approx 85\,000$. A total of 28 HERMES spectra were available, having a typical S/N of 30 in the continuum. Standard reductions including bias and flat-field corrections and wavelength calibrations were performed using the HERMES data reduction pipeline (57). Barycentric corrections were applied.

All spectra were normalized by fitting a piecewise linear function through identified continuum regions selected homogeneously for all datasets. Given the low-amplitude motion of the binary components, stable wavelength calibration is essential. Relative wavelength calibration was brought to a precision of $\approx 0.1 \text{ km s}^{-1}$ by cross-correlating the interstellar sodium lines Na I $\lambda\lambda 5890, 5896$ in the FEROS, HERMES, and ESPaDOnS spectra with a selected ESPaDOnS spectrum (which is wavelength-calibrated). However, this was not possible for the LNA spectra, which do not cover these lines. We therefore consider the RVs of the LNA data as less reliable, and allow for a systematic RV shift between them and the other datasets (see below).

For the spectral analysis, we append the optical spectra with a set of UV spectra retrieved from the Mikulski Archive for Space Telescopes (MAST). The data were acquired with the International Ultraviolet Explorer (IUE) (program IDs: WRJSH, JA017; PIs: Heap, Willis, respectively) and presented previously (58, 59). The spectra cover 1150 – 2150 Å at a resolving power of $R \approx 10\,000$. There are substantial changes in P-Cygni lines that occur over short and long timescales (58, 59). We use a co-added spectrum formed from 20 high-cadence IUE spectra obtained consecutively on 1988 February 3, 4, and 5 for 36 hr. The individual spectra have a S/N of 5-6, such that the co-added spectrum has a total S/N of ≈ 20 . While the process of co-adding smears the small-amplitude variability of the Wolf-Rayet component on the 5 hr

period (see below), the impact is negligible compared to the spectral resolution. Since we only use this spectrum to estimate the effective temperature of the Wolf-Rayet component and analyze the SED, the process of co-adding the data has no impact on our results. The spectrum is normalized using the model continuum obtained from the SED analysis (see below).

For the analysis of the SED, we also retrieved from MAST a far-UV spectrum covering the spectral range 900 – 1200 Å obtained with the Far Ultraviolet Spectroscopic Explorer (FUSE), which have also been previously described (60). The spectrum was acquired on 2001 Mar 5 (PI: Willis, program ID: P224), has a resolving power of $R \approx 20\,000$, and a S/N of ≈ 100 . Since the FUSE and IUE spectra overlap, we use the IUE spectra to calibrate the FUSE spectrum rather than the standard flux calibration, such that the overlapping regions ($\approx 1150 - 1200$ Å) of the IUE spectra and FUSE spectra agree, resulting in a multiplicative factor of 0.8 of the FUSE spectrum. For the SED analysis, we append the FUSE and IUE spectra with a low-resolution flux calibrated IUE spectrum obtained on 1982 Sep 06 (PI: Stickland, ID: EI273), which covers the range 1850 – 3350 Å at a resolving power of $R \approx 500$ and $S/N \approx 5$.

Finally, for the SED analysis, we use U photometry (61), BV photometry (62), JHK photometry (63), and Wide-field Infrared Survey Explorer (WISE) photometry (64).

Analysis of the spectropolarimetric data

Stokes V variations are detected in all ESPaDOnS spectra in multiple lines attributed to the Wolf-Rayet component (Fig. 2), most prominently lines of He II and lines of highly ionized elements. Most lines are in emission in the intensity spectrum, although O v $\lambda 5114$ appears in absorption. No similar Stokes V features are observed in the narrow absorption lines belonging to the B7 V component (Fig. 2I). Since the four individual ESPaDOnS Stokes V spectra obtained during the two observing nights do not show notable variability in the context of the magnetic properties, they were co-added to achieve a higher S/N.

The circular polarization features are qualitatively consistent with the Zeeman effect due to the presence of a strong magnetic field in HD 45166. While the features exhibit some morphological diversity (Fig. 2), they are all - except for O v λ 4930 - of the same polarity, with positive circular polarization observed in the blue wing, and negative polarization observed in the red wing. O v λ 4930 is a weak emission line that appears distinct from the other emission features, with a polarity opposite to that of all other lines in the spectrum (Fig. 2D).

The O v λ 5114 and 4930 lines indicate the magnetic nature of the Wolf-Rayet component and provide quantitative information about its magnetic field. Both lines exhibit resolved Zeeman splitting into triplets that correspond in wavelength to the locations of the extrema and inflection points of their associated Stokes V features. Their narrow profiles, and the pure absorption profile of the O v λ 5114 line, indicate that they form in or close to the stellar surface. The inverted Stokes V signature of O v λ 4930 can be explained by the Zeeman effect operating on a spectral line formed in emission, and not in absorption. As discussed previously (65) for the strongly magnetic O-type star NGC 1624-2, spectral lines of hot stars can form in emission under non-LTE conditions even in or close to the stellar surface.

To quantify the strength and geometry of the detected magnetic field, we measured the mean magnetic field modulus $\langle B \rangle$ and mean longitudinal magnetic field $\langle B_z \rangle$ from the O v λ 5114 and 4930 lines. We renormalized the two lines to the local continuum. We measured the mean field modulus by fitting Gaussians to the three components of each Zeeman triplet to measure the average separation between the two polarized line components and the unpolarized line, $\Delta\lambda_{\text{Zeeman}}$. We then compute $\langle B \rangle = \Delta\lambda_{\text{Zeeman}} / (4.67 \times 10^{-13} g_l \lambda_0^2)$, where $g_l = 1.0$ is the theoretical Landé factor of the line and $\lambda_0 = 4930 \text{ \AA}$ or 5114 \AA is the rest wavelength. We find $\langle B \rangle_{\text{qWR}} = 44.1 \pm 2.0 \text{ kG}$ and $\langle B \rangle_{\text{qWR}} = 41.8 \pm 1.0 \text{ kG}$ for the O v λ 4930 and λ 5114 lines, respectively. The shallow depths of the two O v lines and uncertainty in the positioning of the continuum leads to systematic errors that are not included in the formal 1σ uncer-

ainties provided, which we thus ignored when computing the mean and standard deviation: $\langle B \rangle_{\text{qWR}} = 43 \pm 2.5 \text{ kG}$. We measured a mean longitudinal field of $\langle B_z \rangle_{\text{qWR}} = 16.1 \pm 2.0 \text{ kG}$ and $\langle B_z \rangle_{\text{qWR}} = 11.1 \pm 1.0 \text{ kG}$ for the O v $\lambda 4930$ and $\lambda 5114$ lines, respectively, using the first-order moment method (66), adopting the same Landé factor and rest wavelengths. Taking the mean and standard deviation yields $\langle B_z \rangle_{\text{qWR}} = 13.5 \pm 2.5 \text{ kG}$. As before, we do not weigh the values by the errors due to unaccounted systematic errors.

We also extracted Least-Squares Deconvolution (LSD) mean profiles of the B7V companion (Fig. S1). We employed a standard solar abundance B7 line mask (10) and used the iLSD code (67, 68). From the LSD profile we determined the detection probability in both Stokes V and the diagnostic null (both non-detections), and determined the upper limit of the star’s mean longitudinal magnetic field [$< 60 \text{ G}$ at 3σ confidence; (66)].

We perform a more general comparison between the Stokes I and V spectra of the Wolf-Rayet component and NGC 1624-2 (Fig. S2). NGC 1624-2 is a magnetic star showing the Of?p phenomenon (23, 24) with a very strong magnetic field of $\approx 20 \text{ kG}$ (65), sufficiently large to produce marginal Zeeman splitting of some Stokes I and Stokes V profiles of some individual spectral lines. The star is known to have a large, dense magnetosphere (69, 70). The lower effective temperature of NGC 1624-2 of $35 \pm 2 \text{ kK}$ (65) leads to absorption lines of He I in its spectrum. As a consequence, essentially all H and He I lines, whether in emission or absorption, show Zeeman signatures. In HD 45166, however, no Zeeman signature associated with He I lines is seen, even though He I lines are present (in emission) in its spectrum (Fig. 2H). Instead, Zeeman signatures are detected in association with numerous lines of highly ionized light elements, in particular C IV, N IV, N V, and O v. Another difference is in the ratio of the He II $\lambda 4686$ line to the $\text{H}\alpha + \text{He II } \lambda 6560$ blend. While the $\text{H}\alpha + \text{He II } \lambda 6560$ blend is of similar strength in both stars, the He II $\lambda 4686$ line is almost 20 times stronger in the Wolf-Rayet component of HD 45166, indicating that it is helium rich.

The observed properties of the magnetic field in the Wolf-Rayet component are similar to those found in other hot magnetic stars with dipolar magnetic fields (26), indicating that the Wolf-Rayet component of also hosts a global magnetic field. In this configuration, the polarized flux is largely generated near the stellar surface, where the magnetic field is strongest. As in other magnetic star, the emission lines then originate from stellar wind trapped by the closed magnetic loops (the magnetosphere). The Stokes- V Zeeman signature is produced predominantly in the surface layers of the star. This is because the Zeeman signature is seen only in high ionization lines, which are formed in or close to the stellar surface according to the model atmospheres computed for the star (see below). At larger radial extent, no or weak Zeeman signature is seen, both because the magnetic field strength rapidly drops radially ($\propto r^{-3}$ in a dipolar field, r being the radial distance), and because the signature is diluted in the larger emitting volume, which exhibits opposing polarities. While some contribution to the observed circular polarization could be produced by field lines extending into the star’s wind, the lack of any circular polarization detected in the emission lines of He I indicates that such contributions are very small. In Fig. S3 we show LTE polarized spectrum synthesis calculations with the ZEEMAN code (51, 71, 72) for the O v $\lambda 5114$ line, adopting a dipolar magnetic field of 45 kG with the magnetic field axis parallel to Earth’s line-of-sight. The narrow Zeeman components constrain the non-thermal line broadening to $\lesssim 10$ km/s. In Fig. S3 we have adopted a Doppler width of 6 km/s to account for rotational and turbulence broadening. Although we have adopted a simplified magnetic geometry, the Stokes I and V profiles are reproduced by this basic model.

The Stokes V spectrum thus indicates that the underlying intensity spectrum of the Wolf-Rayet component, which is largely hidden behind the magnetosphere, is characterized by the presence of lines belonging to highly ionized species such as N v, O v and the lack of lower-ionization lines such as He I and O III. To fulfill such conditions, the Wolf-Rayet component needs to be hot ($T_* \gtrsim 45$ kK), consistent with our spectral analysis (see below).

Spectral analysis

To derive the stellar parameters of the components, we use the non-LTE Potsdam Wolf-Rayet (POWR) model atmosphere code (27, 28, 52, 73), which performs radiative transfer in an expanding atmosphere. Models are defined by the chemical abundances, the surface effective temperature T_* , the bolometric luminosity L , the surface gravity g , and wind parameters such as the mass-loss rate \dot{M} and terminal wind speed v_∞ . The radius R_* is given by the Stefan-Boltzmann relation, $R_* \propto \sqrt{L} T_*^{-2}$. In POWR, the effective temperature is defined with respect to a continuum Rosseland optical depth of $\tau_{\text{Ross}} = 20$ as a proxy for the hydrostatic layers. These layers are deeper than the photosphere ($\tau_{\text{Ross}} = 2/3$), at which the photospheric effective temperature T_{eff} is defined. For a star with a negligible wind (such as the B7 V component), $T_* \approx T_{\text{eff}}$. For the Wolf-Rayet component, however, T_{eff} is the effective temperature with respect to a layer that is embedded in the circumstellar material. Hence, we use T_* when comparing to evolution models.

In the subsonic regime, the density is determined by hydrostatic equilibrium. In the supersonic regime, the radial velocity field is assumed to follow a β -law (74), and the density follows from the continuity equation. The supersonic domain does not impact our analysis, since the wind of the B7 V component is negligible, and since the emission features of the Wolf-Rayet component are ignored. In the main non-LTE iteration, the line profiles are assumed to have a constant Doppler width of 30 km s^{-1} . During the integration, the Doppler widths are determined from the depth-dependent thermal broadening and microturbulence ξ (75).

Analysis of the B7 V component

Atmospheric abundances of the B7 V component are fixed to solar (76), which is consistent with the data. The surface gravity of the B7 V component cannot be determined, since the diagnostic Balmer lines are entangled with magnetospheric emission and absorption originating in the

Wolf-Rayet component in a non-trivial manner. We therefore assume $\log g / \text{cm s}^{-2} = 4.0$ (47); varying $\log g$ by 0.2 dex has little impact on the remaining diagnostic lines. Wind parameters are set to negligible values given the lack of wind diagnostics. Microturbulence is set to $\xi = 5 \text{ km s}^{-1}$. We determine T_* and the overall light contribution of the B7 V component in the V -band, $I_B(V)$, using diagnostic lines of O I, Mg II, and Si II, avoiding He I due to possible cross-contamination by the magnetosphere of the Wolf-Rayet component (Fig. S4). The projected rotational velocity $v \sin i$ and macroturbulent velocity v_{mac} are derived using a Fourier method (77), implemented by the IACOB-BROAD tool (78–80). However, in the domain where $v \sin i$ is small, this method is known to lead to degeneracies (79), and we therefore only provide upper limits in Table S1. The rotation and macroturbulence are accounted for by convolving the synthetic spectrum of the B7 V component with corresponding rotational profiles with the value corresponding to the upper limit given in Table S1. the projected rotational velocity of the B7 V component ($v \sin i \lesssim 10 \text{ km s}^{-1}$) is low for this spectral type (81), though other comparably slow rotators exist. While a pole-on configuration of the rotational axis of the B7 V component would provide an explanation for this, such a configuration would not be consistent with the orbital inclination derived below ($i = 49 \pm 11^\circ$), unless it the orbital and rotational axes are misaligned. More likely, the B7 V star is intrinsically a slow rotator.

Analysis of the Wolf-Rayet component

For the Wolf-Rayet component, we adopt previously derived elemental abundances for He, C, N, and O (19); $X_{\text{He}} = 0.67$, $X_{\text{C}} = 0.0059$, $X_{\text{N}} = 0.002$, and $X_{\text{O}} = 0.0015$, which leaves $X_{\text{H}} = 0.32$ (values are mass fractions of the respective element). The remaining abundances are set to solar. Implications of this abundance pattern have been discussed previously (19); it is anomalous compared to either Wolf-Rayet stars or central stars of planetary nebulae. However, these abundances were derived assuming that the emission features stem from a radially expand-

ing outflow, disregarding the magnetic confinement of the wind. We therefore refrain from interpreting the abundances quantitatively. Unlike the previous investigation (19), we rely solely on the iron forest in the UV, which form in the stellar surface and are not contaminated by the magnetosphere. For this purpose, the co-added IUE spectrum is used, which is normalized using the added model continua of both stars. We adopt a mass-loss rate of $\log \dot{M}/(M_{\odot} \text{ yr}^{-1}) = -9.0$ for the Wolf-Rayet component; The high mass-loss rate of $\log \dot{M}/(M_{\odot} \text{ yr}^{-1}) = -6.7$ previously derived (19) was a consequence of ignoring the magnetosphere, so we do not adopt it. We use regions dominated by lines belonging to Fe IV, V, VI (Fig. S5). By using the UV lines, the contribution of the B-type companion is negligible (see SED analysis below). The narrow absorption features in the visual imply a combined projected rotational velocity and microturbulence $v \sin i, \xi \lesssim 10 \text{ km s}^{-1}$, and we adopt these upper limits for the computation of the spectrum. The low projected rotational velocity of the Wolf-Rayet component can be understood as a consequence of angular momentum loss via the magnetic field (82, 83). From the iron forest, we determine $T_{*} = 56 \pm 5 \text{ kK}$, which is lower than the value of 70 kK derived previously (19) by analyzing magnetospheric features using a wind model.

Spectral energy distribution and age

Using the POWR models of the two components and their light ratio in the visual, we compute the luminosities and reddening by fitting the multiwavelength SED to the sum of the models (Fig. S6). We use a reddening law (84) with a total-to-selective extinction ratio of $R_V = 3.1$. We find $\log L_{\text{qWR}}/L_{\odot} = 3.830 \pm 0.050$ and $\log L_B/L_{\odot} = 2.250 \pm 0.050 [L_{\odot}]$, with a color excess of $E_{B-V} = 0.210 \pm 0.010$, which is consistent with the strength of the interstellar lines (e.g., Ly α). The parameters derived for the B-type component are consistent with its spectral type (47). A flux excess is noted in the infrared which grows gradually between $2 \mu\text{m}$ and $22 \mu\text{m}$; it could originate in free-free emission stemming from the trapped outflow, which is not

included in our model.

We used the BONNSAI Bayesian tool (29, 85) to estimate the current mass and age of the B-type component using single-star evolution tracks (39), using our derived T_* , $\log L$, and $v \sin i$ as input parameters. We find a mass of $M_B = 3.38 \pm 0.10 M_\odot$ and an age of 105 ± 35 Myr, which we consider as the age of the binary.

TESS light curve and the 1.6 d period

To analyze the light curve of HD 45166, we downloaded 15×15 pixel cutouts from the TESS full frame images (FFIs) stored at MAST using the ASTROCUT package (86). We extracted light curves for HD 45166 by defining custom aperture masks, and estimated the background flux from the median flux per frame excluding pixels that contain stellar flux. We subtracted the background flux from the target flux, normalized by dividing through the median. A final linear trend was subtracted from each light curve to remove remaining instrumental effects. Our FFI-extracted light curves for sectors 6 and 33 are shown in the left panel of Fig. S7A and B.

To determine the variability in each light curve, we used Fourier analysis and the method of iterative pre-whitening (87). We fit the light curve of each sector with a model function of the form:

$$\Delta m(t) = \sum_i A_i \cos(2\pi \nu_i (t - t_{\text{ref}}) + \phi_i), \quad (\text{S1})$$

where t is the time stamps of the light curve with units of BJD–2457000.0, with BJD being the Barycentric Julian date (preferred over MJD for high-precision space-mission photometry), t_{ref} is a reference time at the end of the light curve of each sector ($t_{\text{ref}} = 1490.0$ and 2225.0 for sectors 16 and 33 in units of BJD-2457000.0, respectively), and ν_i , A_i , and ϕ_i are the frequency, amplitude, and phase of the i^{th} cosinusoid term, respectively.

To determine the total number of significant frequencies, we use a significance criterion of

an amplitude signal-to-noise ratio (S/N) larger than four in the amplitude spectrum, where the signal is defined as the amplitude of a peak and the noise is defined as the average amplitude in the residual amplitude spectrum in a symmetric window of width 1 d^{-1} centered at the extracted peak for each iteration (87). In total, we detected two and three frequencies fulfilling our significance criterion in the sectors 6 and 33 TESS data of HD 45166, respectively. We performed an independent multi-frequency non-linear least-squares fit to each light curve using Eq. (S1) to optimize the frequencies and their corresponding amplitudes and phases, and determine correlated uncertainties, which are provided in Table S2.

The shorter 10-min cadence of the sector 33 data yields a lower noise level in the amplitude spectrum, on average, because of the factor three larger number of data points compared to the sector 6 data. This contributes to the detection of the additional frequency in the sector 33 TESS data, and the overall smaller uncertainties for the optimized parameters in Table S2. Given the low frequency resolution of a short (27 d) TESS light curve of $1/\Delta(t) \simeq 0.04 \text{ d}^{-1}$, the two lower frequencies in sector 6 are the same as those in sector 33.

Multi-periodic variability in a period range of several days is typical of gravity mode pulsations in main-sequence B-type stars (88). The dominant frequency of $\approx 0.6 \text{ d}^{-1}$ lies close to the period of 1.66 d detected from RV variations for the B-type component [(16), see also below]. We infer that the 1.6 d period, previously attributed to the orbital period of the system, is instead due to pulsations in the B7 V component. This is consistent with the much longer orbital period we find below.

Revised orbital analysis of HD 45166

To measure the RVs from the available spectra, we cross-correlate the observations with appropriate templates, following an established procedure (89). Measuring the RVs of the B-type component is only possible with the FEROS, HERMES, and ESPaDOnS spectra given the lower

wavelength coverage and quality of the LNA spectra. To form the template of the B7 V component, we first use the synthetic POWR model (Fig. S4). We then shift-and-add all observations using the measured RVs, and use this to produce a calibrated template of co-added observations (90). The new template is then cross-correlated with the observations to yield the final absolute RVs of the B7 V component. We use the strong absorption lines Si II $\lambda\lambda$ 4128, 4131 and Mg II $\lambda\lambda$ 4481.1, 4481.3 for the cross-correlation, and find that our conclusions do not depend on the choice of lines.

For the Wolf-Rayet component, we use a similar procedure. However, lacking a synthetic template, we use one of the FEROS observations as a first template. We use the emission-line complex in the range 4630–4660 Å for cross-correlation. After measuring the preliminary RVs, which are measured relative to the observation used as a template, we form a co-added, high S/N template to remeasure the RVs. We allow for an overall systematic shift between the RVs of the Wolf-Rayet and B7 V components, such that they result in the same systemic velocity (see below). The choice of emission lines used for cross-correlation does not affect our results, though usage of highly variable lines such as He II λ 4686 yields a substantially larger scatter, and is therefore avoided. A total of 199 and 96 RVs for the Wolf-Rayet and B7 V components are available. An overview of the derived RVs is shown in Fig. S8, and they are also provided as supplementary data (table S1).

Both components exhibit substantial variability on several timescales, and this variability appears to be associated with several periods, consistent with previous investigations (16). The RVs of the B7 V component vary on a short timescale, and we can confirm the 1.6 d period found previously (16) and formerly attributed to the orbital period of the system. By subtracting several periods from the RVs measured for the Wolf-Rayet component, the 1.6 d period was previously found (16) in the Wolf-Rayet component as well. However, having repeated this experiment using our dataset, we do not confirm this result. Instead, we find that the 1.6 d period

is associated with non-radial gravity-mode pulsations in the B7 V component (see above). This is evident in the ESPaDOnS spectra, which have pronounced variability between the two observing nights. To boost the S/N, we co-added all observations acquired during a single night, and show the resulting spectra in Fig. S9. This spectral variability is typical for non-radial gravity-mode pulsations in slowly rotating stars (91).

The strong emission lines of the Wolf-Rayet star display variability with a short period of the order of 5 hr, as previously identified (16). The origin of this period, which persists pseudo-periodically for at least 20 yr, is not clear. However, this period cannot correspond to orbital motion, since the associated RV semi-amplitude is ≈ 1 to 2 km s^{-1} and varies from epoch to epoch. The combination of a 5 hr period with the low RV amplitude would either imply a highly unlikely pole-on geometry, or a sub-stellar mass for the companion, which is inconsistent with stellar evolution. It is possible that the 5 hr period is due to pulsations in the Wolf-Rayet component, in a phenomenon related to its magnetic field, or in an interplay between the two.

Upon inspection of the long-term variability of the RVs of both components, anti-phase motion between the two components is apparent. While the short-term variability partly masks this trend, we conclude that the two stars are bound on a long-period orbit. In the HERMES and ESPaDOnS observations taken during 2019-2022, the RVs of the B7 V component in Fig. S8 are persistently red-shifted with respect to those of the Wolf-Rayet component. However, exactly the opposite is seen in the FEROS spectra, acquired in 2002. The individual HERMES observation taken in 2012 again shows a reversal of the RVs.

To obtain an orbital solution, we binned the RVs on a 30 d baseline to smooth-out short-term variability in the two components. To account for the short-term variability, we attribute an additional uncertainty of 3 km s^{-1} to the individual measurements (representative of the amplitude of the short-term RV variation), but divide this by the number of measurements per 30 d bin, though we require the uncertainties to remain at least 1 km s^{-1} . We fitted the binned

RVs with a model of the RV curve resulting from the orbital parameters ($P, t_0, e, \omega, K_1, K_2, v_0$) using the Python `lmfit` package (92, 93). We also included a systematic shift between the RVs of the Wolf-Rayet component and a systematic shift of the LNA RVs (see above). The LNA offset is found to be $-2.8 \pm 1.6 \text{ km s}^{-1}$, which is small and does not impact our solution. The solution is shown in Fig. 4, which corresponds to the parameters given in Table S1. The derived period is 22.5 yr, though this value depends on the treatment of the uncertainties. The formal uncertainties on the orbital parameters are derived from the covariance matrix; a Markov Chain Monte Carlo (MCMC) simulation yielded similar uncertainties.

While the ratio K_2/K_1 yields $q = 0.58 \pm 0.16$, we can determine the mass ratio independently of the orbital elements by considering that, at each point of time, the RVs of the components scale in proportion to their semi-amplitudes (94):

$$\text{RV(B)} = -q \cdot \text{RV(qWR)} + C, \quad (\text{S2})$$

where RV(B) and RV(qWR) are the RVs of the B7 V and Wolf-Rayet components at a given epoch, respectively, $q \equiv M_{\text{qWR}}/M_{\text{B}}$ is the mass ratio, and C is a constant that depends on the systemic velocities and q . By performing a linear regression to the measurements (Fig. S10), we find $q = 0.60 \pm 0.13$, which agrees well with the value derived from the orbital analysis.

The evolutionary mass of the B7 V component, in combination with the mass ratio, leads to the mass of the Wolf-Rayet component. Using our derived evolutionary mass of $M_{\text{B}} = 3.38 \pm 0.10$ and the derived mass ratio of $q = 0.60 \pm 0.13$ yields $M_{\text{qWR}} = 2.03 \pm 0.44 M_{\odot}$. From $M_{\text{B}} \sin^3 i = 1.50 \pm 0.74 M_{\odot}$ and $M_{\text{B}} = 3.38 \pm 0.10$, we infer $i = 49 \pm 11^\circ$. The long period of the system provides an explanation for the low RV amplitudes observed in the system, without the need to invoke a pole-on configuration. We find that the Wolf-Rayet component exceeds the Chandrasekhar mass limit, and is expected to undergo core-collapse (see below).

Evolutionary scenario

Assuming that the Wolf-Rayet component formed through a merger of two helium stars (see main text), we construct an evolutionary model for the system using the MESA stellar evolution code (46). We considered the evolution of a $5M_{\odot}$ star with a $3M_{\odot}$ companion at an initial orbital period of two days, representing the inner binary in an initial triple. The more massive component overflows its Roche lobe first, undergoing mass transfer both during and after its main sequence, resulting in a stripped $0.63M_{\odot}$ star. Mass transfer increases the orbital period and separation to 66 days and $138R_{\odot}$, while the accretor mass increases to $7.4M_{\odot}$. Such post-interaction binaries are known to exist (90, 95, 96). Owing to its increase in mass, the accretor evolves faster, finishing its main sequence and initiating a phase of inverse mass transfer before the stripped star depletes core helium. Due to the extreme mass ratio, the mass-transfer is unstable, and the system evolves into a common-envelope phase at an age of 130 Myrs.

The outcome of common-envelope phases is poorly understood in binary evolution (97). One-dimensional models can be used to assess whether a merger would occur, or whether the hydrogen envelope would be ejected before the helium cores would coalesce. We follow an energy prescription for common envelope evolution (44). The binding energy of the envelope down to a given mass coordinate m , $E_{\text{bind}}(m)$, can be computed as

$$E_{\text{bind}}(m) = \int_m^M \left(-\frac{Gm}{r(m)} + u(m) \right) dm, \quad (\text{S3})$$

where M is the total mass of the star, $r(m)$ is the radius of a shell enclosing the mass m , G is the gravitational constant, and u is the specific internal energy of the star, for which we also consider the energy from hydrogen and helium recombination. The source of energy to unbind this material is the change in orbital energy. To estimate the orbital energy released through a merger we consider that all layers above m are ejected from the donor, and compute the orbital separation a_{RLOF} at which the stripped star (with a radius of $0.18R_{\odot}$ at the onset of common-

envelope) would overflow its Roche lobe. The energy released through the merger, $E_{\text{merger}}(m)$, is computed then from the orbital energy at this separation,

$$E_{\text{merger}}(m) = \frac{GmM_{\text{stripped}}}{2a_{\text{RLOF}}(m)}, \quad a_{\text{RLOF}}(m) = \frac{0.18 R_{\odot}}{f(M_{\text{stripped}}/m)} \quad (\text{S4})$$

where M_{stripped} is the mass of the original primary after it has been stripped and

$$f(q) = \frac{0.49q^{2/3}}{0.6q^{2/3} + \ln(1 + q^{1/3})} \quad (\text{S5})$$

is an approximation of the Roche radius (98). The layers that are ejected through the common envelope phase are then determined from the condition $E_{\text{bind}}(m) = \alpha_{\text{CE}}E_{\text{merger}}(m)$, where $\alpha_{\text{CE}} \in [0, 1]$ is the efficiency of converting the orbital energy into ejection of the material.

The binding energy of the donor star and the energy that would be released through a merger after ejecting all material above a given mass coordinate are shown in Fig. S11. If orbital energy converts with full efficiency into removing the envelope ($\alpha_{\text{CE}} = 1$), only $0.08M_{\odot}$ of hydrogen rich material would remain, indicating that the system would eject the common envelope, halting the in-spiral and merging process (Fig. S11). However, the actual efficiency is expected to be lower (99). Taking $\alpha_{\text{CE}} = 0.5$ or 0.25 the system would retain $0.3M_{\odot}$ and $0.62M_{\odot}$ of hydrogen rich material, respectively. We perform a simple model of the post-merger evolution by constructing a star with a composition profile that combines that of the stripped star with the layers that are not ejected from the donor star (Fig. S11). The post-merger evolution depicted in Fig. 5 shows the evolution after the merged object reaches a state of thermal equilibrium as a core-helium burning object, until it reaches core helium depletion.

For the merger model with $\alpha_{\text{CE}} = 0.25$, we find the best match to the properties of the Wolf-Rayet component of HD 45166 occurs at has an age (starting from the initial binary model) of 133 Myrs, consistent (within 1σ) with the age constraint provided by the B7 V component. The surface composition is rich in hydrogen, but due to the CNO cycle it has a very low carbon abundance ($X_C = 6.5 \times 10^{-5}$), which is inconsistent with previous measurements of the system (19).

That analysis used a wind model that does not describe the magnetosphere (see above). However, the observed strength of carbon emission lines (Figs. 1 and 2) in the spectrum indicates that the atmosphere of the Wolf-Rayet component contains a significant amount of carbon, which is inconsistent with our merger model. We argue that fallback from some of the outermost layers of the donor star could have contaminated the merger product with material that has not been CNO processed, leading to higher oxygen and carbon abundances observed at the surface in the present day. While modeling the merger product beyond core-helium depletion is subject to various uncertainties [such as mass-loss in the presence of the magnetic field, (100)], in our model, we find it forms a $1.29M_{\odot}$ O-Ne-Mg core with a $1.04M_{\odot}$ envelope composed primarily of helium and with a small amount ($0.04M_{\odot}$) of hydrogen. We do not model the evolution of the system beyond this point, but we expect the core would continue to grow from shell burning. We predict that the Wolf-Rayet component will become a supergiant ($R \approx 300 R_{\odot}$, well within its Roche lobe) and explode as a type Ib or IIb electron-capture supernova [(101), their table 1], depending on the amount of hydrogen retained (102, 103). The neutron star remnant is expected to possess a magnetic field strong enough to appear as a magnetar (see above).

Supplementary Text

Parallels have been drawn between the spectrum of HD 45166 and Wolf-Rayet stars belonging to the class of V Sagittae stars (104). This class comprises a few stars that portray Wolf-Rayet spectra with reported photometric and spectroscopic variability periods of the order of hours that are attributed to orbital periods. Specifically, WR 7a and WR 46 were proposed to exhibit properties similar to HD 45166 (105, 106). However, both WR 7a and WR 46 exhibit broad, strong emission lines that resemble those of classical Wolf-Rayet stars. Moreover, no firm detection of a magnetic field could be obtained for WR 46 (107). Hence, while an investigation of the magnetic properties of WR 7a might still be worth pursuing, neither WR 7a nor WR 46

appear to be suitable candidates for massive magnetic helium stars.

An intriguing similarity is observed when comparing the spectrum of the Wolf-Rayet component to a subset of central stars of planetary nebulae, classified as [WN] or [WC] stars (108). The spectral appearance and luminosities of some [WC] and [WN] stars matches well with those of the Wolf-Rayet component in HD 45166. However, a distinct difference is that HD 45166 has no nebula associated with it (58): no evidence for nebulosity is seen in the spectrum, nor is it seen in infrared images. While central stars of planetary nebulae are thought to represent the final evolutionary stages of solar-type stars following a “standard” post-asymptotic giant branch evolution, it is possible that a few impostors are hidden in this population. In the context of the evolutionary scenario proposed here, their nebulae could be the remnant of a violent merger event, implying that they are “freshly born” magnetic helium stars. Specifically, a few such objects were identified that share a similar spectral morphology to HD 45166, and notably the $\text{O}^?p$ emission complex in the range 4630-4660 Å. Examples include PB 8 (108) and Hen 2-108. However, a campaign to measure the magnetic fields of a sample of central stars of planetary nebulae, including Hen 2-108, did not find evidence for magnetism in these objects (109). It remains to be seen whether other [WN] or [WC] stars exhibit strong magnetic fields.

Supplementary Figures

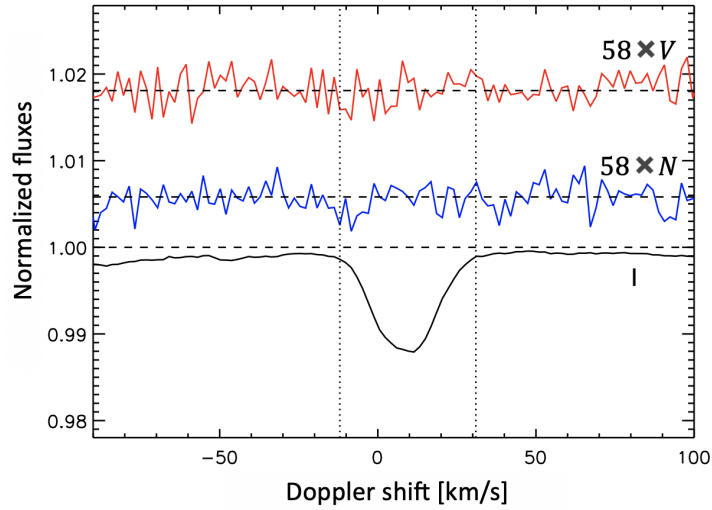


Figure S1: **LSD profile of the B7 V companion.** The lower (black) curve is the mean Stokes I profile. The upper (red) curve is the measured net circular polarization (Stokes V). The middle (blue) curve is the diagnostic null N . No signal is detected inside or outside the line range in either V or N . The vertical dashed lines indicate the integration range used for measurement of the detection probability and longitudinal magnetic field.

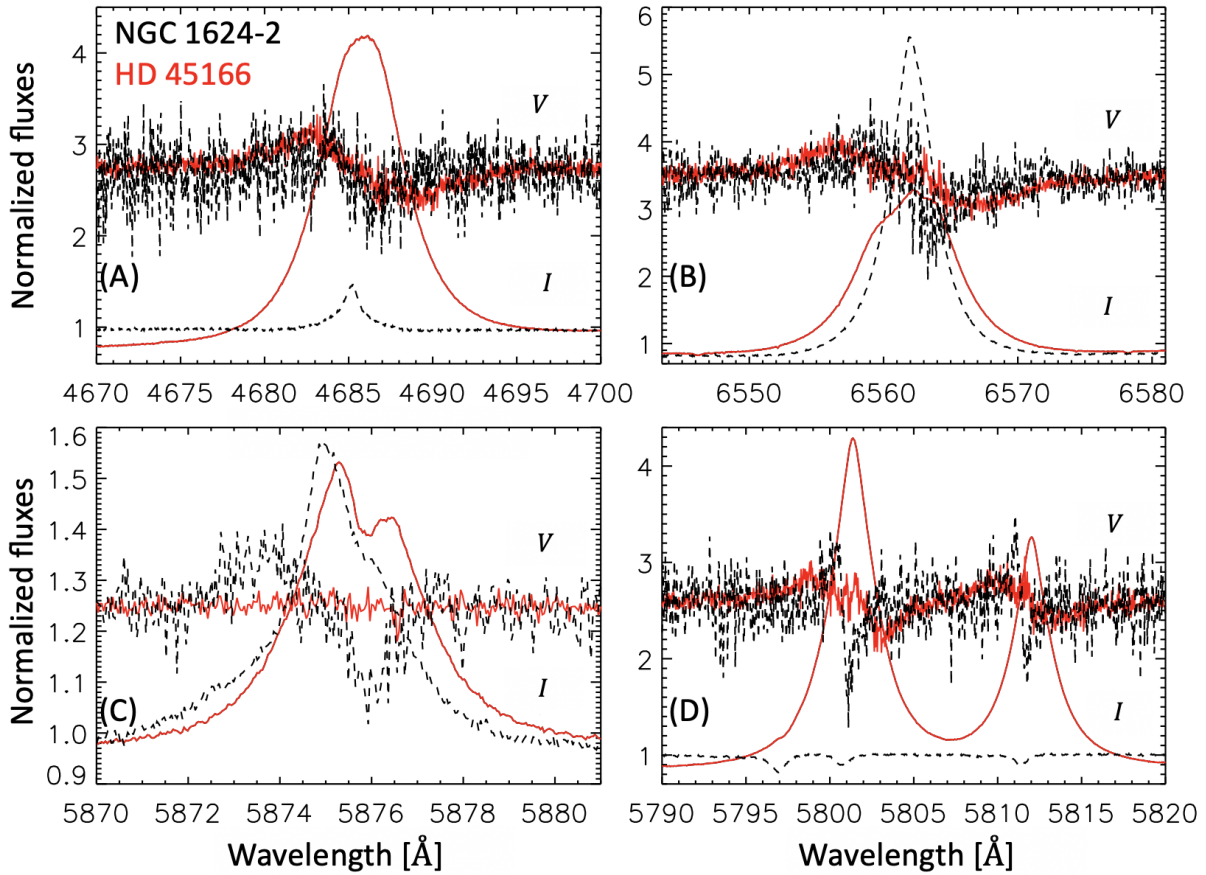


Figure S2: **Comparison between HD 45166 and NGC 1624-2.** Shown are Stokes I and V line profiles (see labels in panels) in spectra of HD 45166 (red/solid) and NGC 1624-2 (black/dashed) for He II λ 4686 (A), H α + He II λ 6560 (B), He I λ 5876 (C), and C IV $\lambda\lambda$ 5801, 5811 (D).

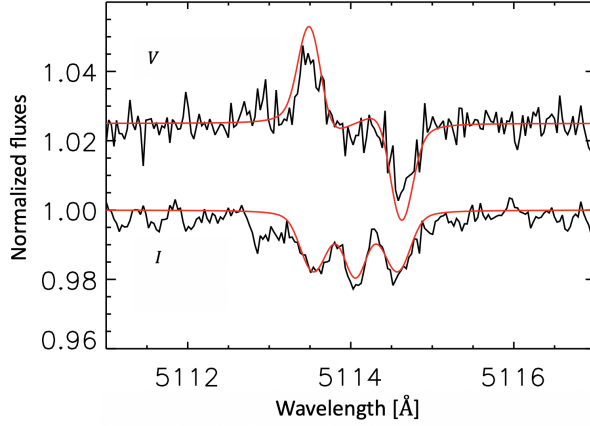


Figure S3: **Modeling of the spectropolarimetric signature.** Shown are Stokes I and V profiles of O v λ 5114 (black) compared to LTE polarized spectrum synthesis calculations (red) computed assuming a pole-on magnetic dipole of polar strength 45 kG. Such a field geometry roughly reproduces the observed profiles.

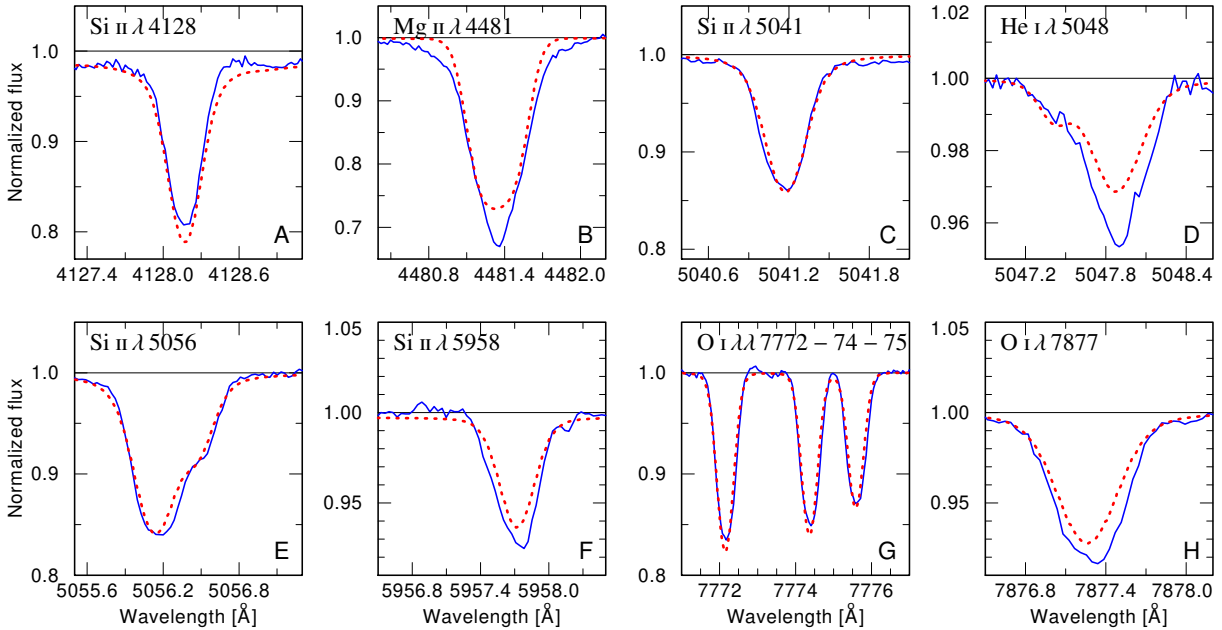


Figure S4: **Spectral analysis of the B7 V component.** Shown is a comparison between our composite spectral model of HD 45166 (red) and the co-added ESPaDOnS spectrum (blue), focusing on absorption lines belonging to the B-type component. The composite model includes both the Wolf-Rayet and B7 V components, weighed with their respective wavelength-dependent light ratios. The spectral lines shown are formed only in the B7 V component, with the possible exception of He I λ 5048 (D), which may be contaminated by the magnetosphere of the Wolf-Rayet component. Horizontal black lines are continuum levels.

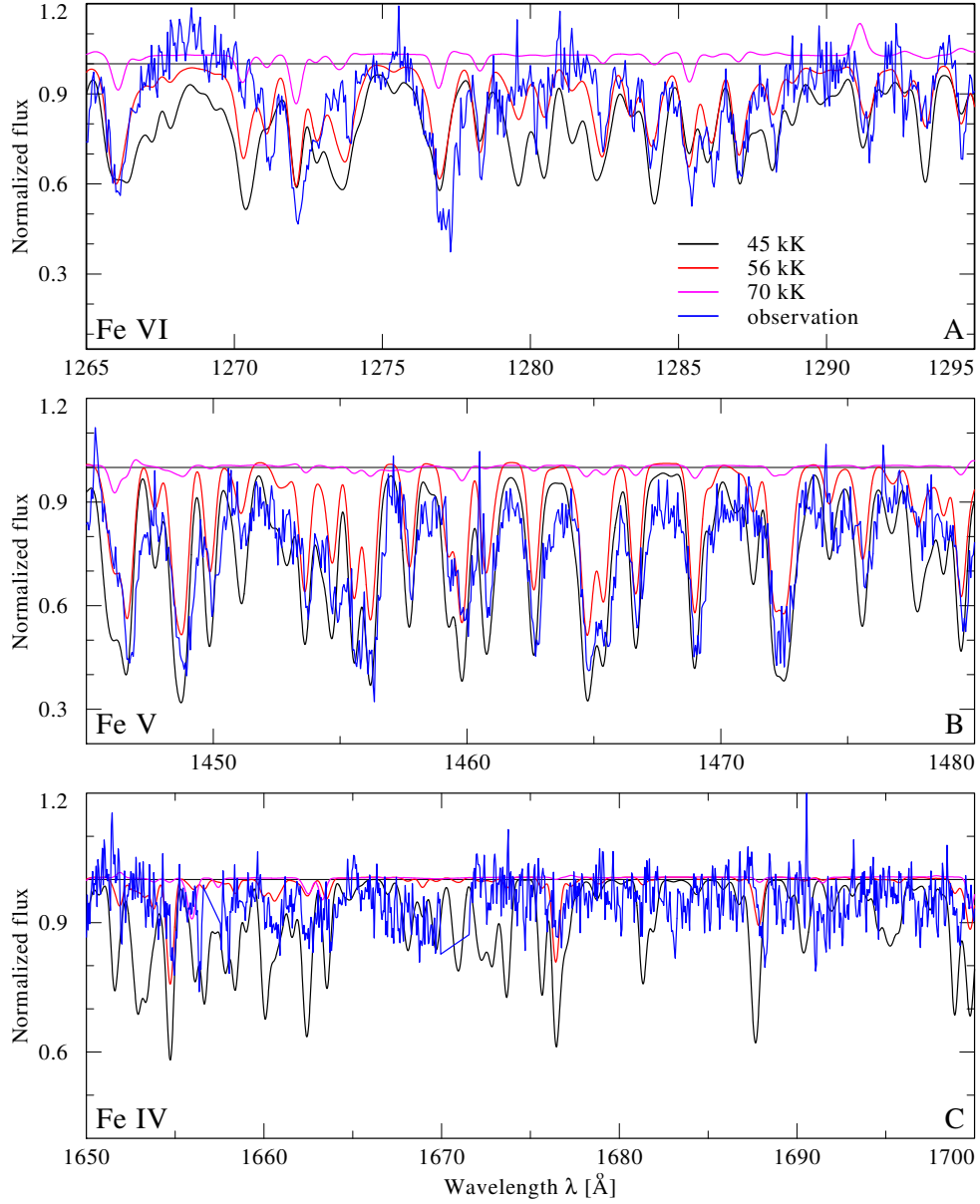


Figure S5: **Spectral analysis of the Wolf-Rayet component.** Shown is a comparison between the co-added IUE spectrum (blue), normalized using the model continua, and three composite POWR models calculated with $T_* = 45, 56,$ and 70 kK (in black, red, and green, respectively) for the Wolf-Rayet component. The panels show regions dominated by Fe VI, v, and IV (panels A, B, and C, respectively). The contribution of the B7 V component is negligible (see Fig. S6). The effective temperature of the Wolf-Rayet component is estimated at $T_* = 56.0 \pm 5.0$ kK.

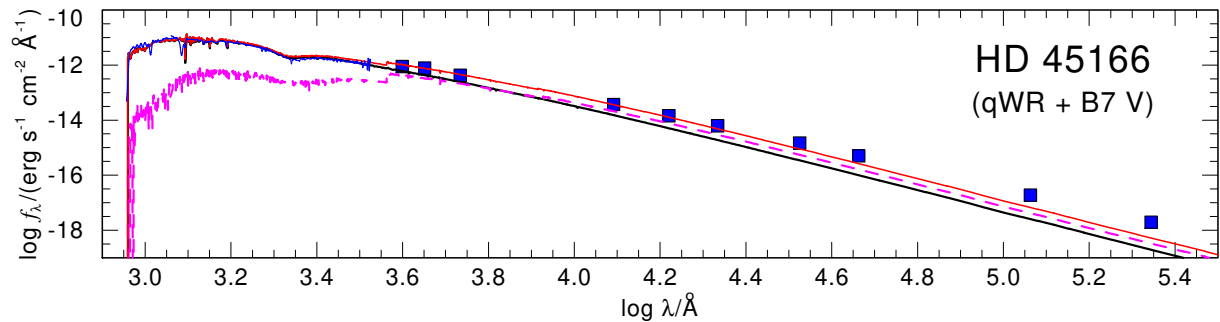


Figure S6: **Spectral energy distribution of HD 45166.** The observed SED (blue line for IUE and FUSE spectroscopy and blue squares for photometry) is compared to the sum (solid red line) of the synthetic SEDs of our models for the Wolf-Rayet component (solid black line) and the B-type component (dashed green line). The Wolf-Rayet component fully dominates the UV flux. The flux excess observed in the infrared could originate in free-free emission stemming from the trapped outflow.

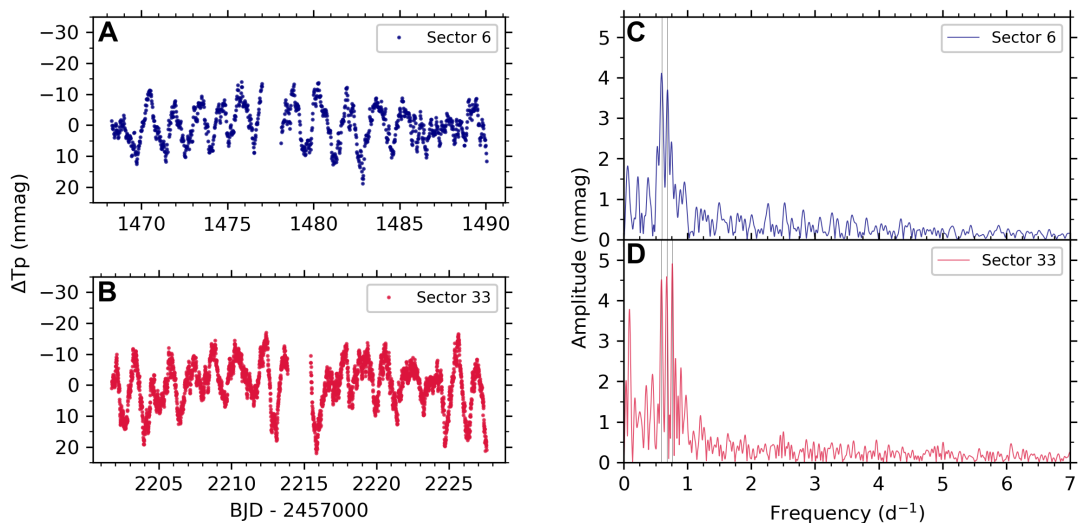


Figure S7: **Frequency analysis of the TESS light curve of HD 45166.** A and B: TESS light curve from sectors 6 (A) and 33 (B) of HD 45166, with relative brightness in units of millimagnitude (mmag) in the TESS passband ΔT_p on the ordinate axis and time (in BJD) on the abscissa. C and D: Amplitude spectra of sector 6 (C) and 33 (D) TESS light curves, with significant frequencies (i.e. exceeding the significance threshold $S/N > 4$; see text for detailed) marked by vertical gray lines.

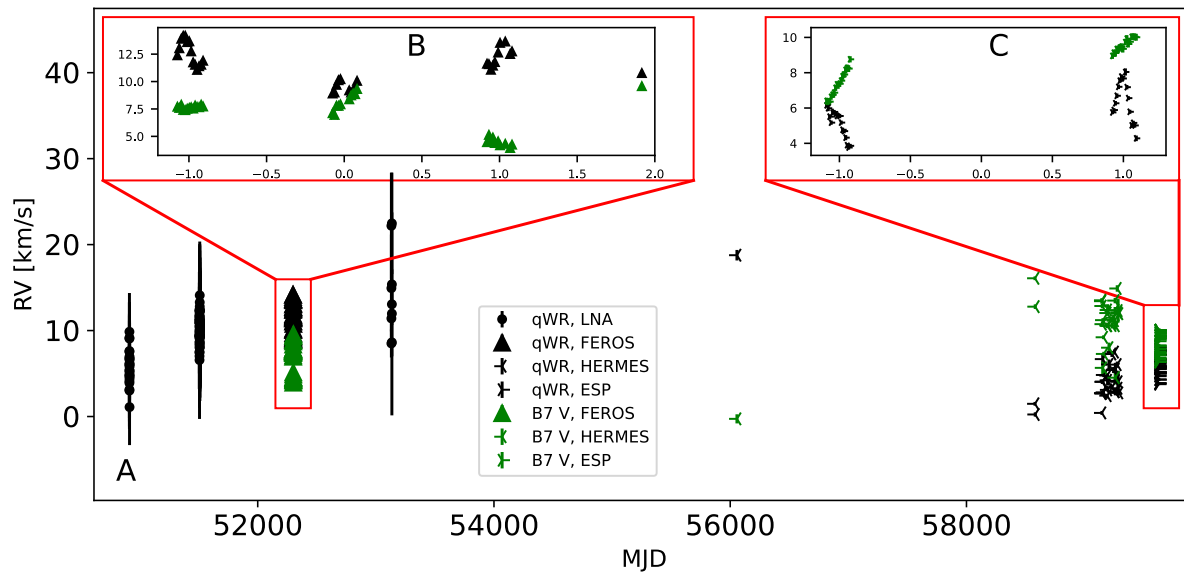


Figure S8: **Overview of RVs measured for the two components of HD 45166.** (A) Black and green symbols show the 199 and 96 RVs derived for the Wolf-Rayet and B7 V components, respectively. Each instrument is marked by a different symbol (see legend). The relative RVs of the Wolf-Rayet component were vertically shifted to have the same mean as the absolute RVs of the B7 V component. (B and C) Short-term variability of both components. The origin of the ≈ 5 hr period of the Wolf-Rayet is uncertain, but could be related to pulsations. We argue (see above) that the ≈ 1.6 d period is due to pulsations in the B7 V component. There is a long-term anti-phase motion of the two components, indicating a period of ≈ 20 years. Error bars depict formal 1σ uncertainties (the uncertainties of HERMES and ESPaDOnS RVs are comparable to symbol sizes).

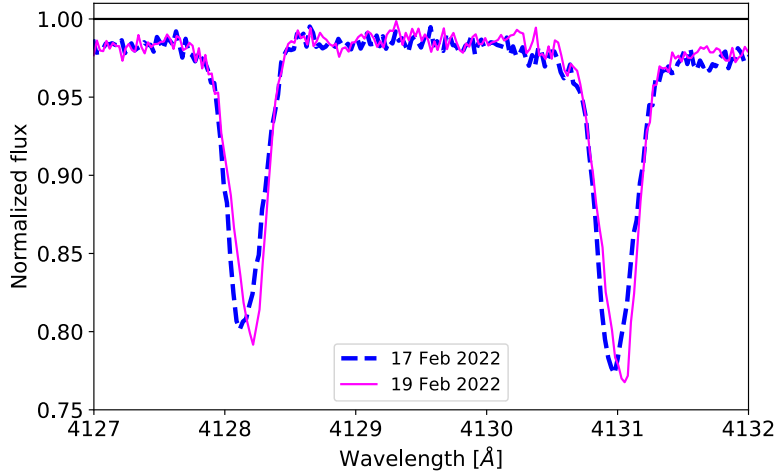


Figure S9: **Spectroscopic signature of gravity-mode pulsations in the B7 V component.** Shown are co-added nightly ESPaDOnS spectra taken during 2022 Feb 17 and 19 Feb 2022, focusing on the Si II λ 4128, 4131 doublet of the B7 V component. There are line profile variations, with their cores shifting in apparent RV, but their wings being static. This behavior is typical for non-radial gravity-mode pulsations (91).

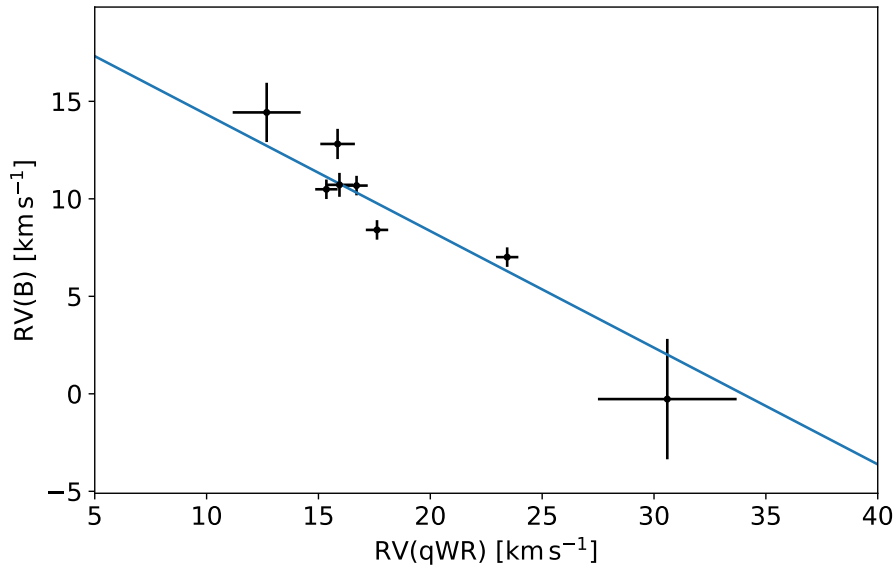


Figure S10: **Derivation of the mass ratio.** The RVs of the B7 V component (y-axis) are shown as a function of those of the Wolf-Rayet component (x-axis). Measurements are the same as those used for the orbital analysis. The line is a linear regression to the data; its negative slope (mass ratio) and intercept are $q = 0.60 \pm 0.13$ and $C = 20.3 \pm 2.3$.

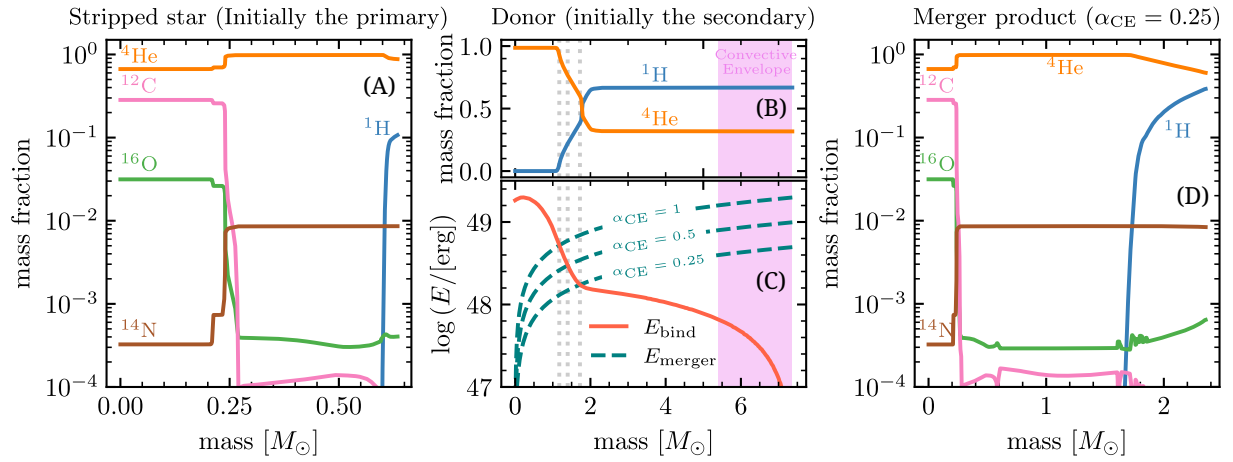


Figure S11: Abundance profiles and envelope binding energy of the pre- and post-merger product. (A) abundance profile of the stripped star immediately before the merger. (B, C) Abundance profile (B) and binding energy (C) of the donor star at the onset of the in-spiral, prior to envelope ejection. Dashed teal curves in panel C show the energy that would be released through a merger after ejecting all material above a given mass coordinate for different efficiencies α_{CE} . The intersection between these curves with $E_{\text{bind}}(m)$, denoted with dashed vertical lines, determines the point to which the donor star would be stripped. (D) abundance profile of the merger product under the assumption $\alpha_{\text{CE}} = 0.25$. Composition profile is constructed from both stars starting from the center with regions depleted in hydrogen in order of increasing helium abundance, and then layers with increasing hydrogen abundance.

Supplementary Tables

Table S1: **Derived parameters for HD 45166.** Provided are the distance, reddening E_{B-V} , age, orbital elements (period P , time of periastron t_0 , eccentricity e , argument of periastron ω , systemic velocity v_0 , semi-major axis a , mass ratio q , orbital inclination i , and RV amplitudes K_1, K_2), mean magnetic-field modulus and line-of-sight components $\langle B \rangle$ and $\langle B_z \rangle$, minimum masses $M \sin^3 i$, masses M , relative contributions to the light in the V -band $l(V)$, effective surface temperatures T_* , luminosities $\log L$, radii R_* , projected rotational velocities $v \sin i$, rotational period P_{rot} , and elemental abundances of He, C, N, and O ($X_{\text{He}}, X_{\text{C}}, X_{\text{N}}, X_{\text{O}}$) in mass fractions. Uncertainties are 68% confidence interval (1σ).

Parameter	unit	B7 V	Wolf-Rayet
Distance (adopted)	parsec	991^{+38}_{-33} (110)	
E_{B-V}	magnitude	0.210 ± 0.010	
age	Myr	105 ± 35	
P	day	8200 ± 190	
t_0 (MJD)	-	49820 ± 360	
e	-	0.46 ± 0.18	
ω	degree	132 ± 11	
v_0	km s^{-1}	5.7 ± 1.8	
a	au	10.5 ± 1.8	
$q \equiv M_{\text{qWR}}/M_{\text{B}}$	-	0.60 ± 0.13	
i	degree	49 ± 11	
K	km s^{-1}	5.8 ± 1.3	9.9 ± 1.6
$\langle B \rangle$	kG	-	43.0 ± 2.5
$\langle B_z \rangle$	kG	< 0.02	13.5 ± 2.5
$M \sin^3 i$	M_{\odot}	1.50 ± 0.74	0.85 ± 0.45
M	M_{\odot}	3.40 ± 0.06	2.03 ± 0.44
$l(V)$	-	0.460 ± 0.050	0.560 ± 0.050
T_*	kK	13.00 ± 0.50	56.0 ± 6.0
$\log L/L_{\odot}$	-	2.250 ± 0.050	3.830 ± 0.050
R_*	R_{\odot}	2.63 ± 0.41	0.88 ± 0.16
$v \sin i$	km s^{-1}	$\lesssim 10$	$\lesssim 10$
P_{rot}	day	-	124.82 ± 0.21
X_{He} (adopted)	-	0.25 (76)	0.67 (19)
X_{C} (adopted)	-	0.0024 (76)	0.0059 (19)
X_{N} (adopted)	-	0.00069 (76)	0.0020 (19)
X_{O} (adopted)	-	0.0057 (76)	0.0015 (19)

Table S2: **Significant frequencies extracted from the TESS light curves of HD 45166.** Frequencies exceeding the significance criterion (25) in sectors 6 (upper part) and 33 (lower part) of the TESS light curve are listed in the first column. The amplitudes and phases are given in the second and third columns (Eq. S1).

	Frequency (d ⁻¹)	Amplitude (mmag)	Phase (radian)
Sector 6:			
	0.6006 ± 0.0012	4.23 ± 0.20	1.618 ± 0.094
	0.6825 ± 0.0014	3.75 ± 0.20	-0.11 ± 0.11
Sector 33:			
	0.59401 ± 0.00056	4.45 ± 0.11	1.114 ± 0.045
	0.67593 ± 0.00057	4.46 ± 0.12	1.622 ± 0.045
	0.75981 ± 0.00054	4.68 ± 0.12	0.142 ± 0.043

Caption for S1 (.xlsx file): **Derived RVs for the two components of HD 45166.** The 1st column lists the instrument, the 2nd column lists the MJD, and 3rd, 4th, 5th, and 6th columns list the RV and the 1 σ uncertainty (in km s⁻¹) for the Wolf-Rayet and B7 V components, respectively.

References and Notes

1. P. A. Crowther, Physical Properties of Wolf-Rayet Stars. *Annu. Rev. Astron. Astrophys.* **45**, 177–219 (2007). [doi:10.1146/annurev.astro.45.051806.110615](https://doi.org/10.1146/annurev.astro.45.051806.110615)
2. N. Langer, Presupernova Evolution of Massive Single and Binary Stars. *Annu. Rev. Astron. Astrophys.* **50**, 107–164 (2012). [doi:10.1146/annurev-astro-081811-125534](https://doi.org/10.1146/annurev-astro-081811-125534)
3. B. Paczyński, Evolution of Close Binaries. V. The Evolution of Massive Binaries and the Formation of the Wolf-Rayet Stars. *Acta. Astron.* **17**, 355 (1967).
4. S. E. Woosley, The Evolution of Massive Helium Stars, Including Mass Loss. *Astrophys. J.* **878**, 49 (2019). [doi:10.3847/1538-4357/ab1b41](https://doi.org/10.3847/1538-4357/ab1b41)
5. E. Zapartas, S. E. de Mink, R. G. Izzard, S.-C. Yoon, C. Badenes, Y. Götzberg, A. de Koter, C. J. Neijssel, M. Renzo, A. Schootemeijer, T. S. Shrotriya, Delay-time distribution of core-collapse supernovae with late events resulting from binary interaction. *Astron. Astrophys.* **601**, A29 (2017). [doi:10.1051/0004-6361/201629685](https://doi.org/10.1051/0004-6361/201629685)
6. V. M. Kaspi, A. M. Beloborodov, Magnetars. *Annu. Rev. Astron. Astrophys.* **55**, 261–301 (2017). [doi:10.1146/annurev-astro-081915-023329](https://doi.org/10.1146/annurev-astro-081915-023329)
7. S. Mereghetti, J. A. Pons, A. Melatos, Magnetars: Properties, Origin and Evolution. *Space Sci. Rev.* **191**, 315–338 (2015). [doi:10.1007/s11214-015-0146-y](https://doi.org/10.1007/s11214-015-0146-y)
8. L. Ferrario, A. Melatos, J. Zrake, Magnetic Field Generation in Stars. *Space Sci. Rev.* **191**, 77–109 (2015). [doi:10.1007/s11214-015-0138-y](https://doi.org/10.1007/s11214-015-0138-y)
9. L. Ferrario, D. Wickramasinghe, Modelling of isolated radio pulsars and magnetars on the fossil field hypothesis. *Mon. Not. R. Astron. Soc.* **367**, 1323–1328 (2006). [doi:10.1111/j.1365-2966.2006.10058.x](https://doi.org/10.1111/j.1365-2966.2006.10058.x)
10. G. A. Wade, C. Neiner, E. Alecian, J. H. Grunhut, V. Petit, B. Batz, D. A. Bohlender, D. H. Cohen, H. F. Henrichs, O. Kochukhov, J. D. Landstreet, N. Manset, F. Martins, S. Mathis, M. E. Oksala, S. P. Owocki, T. Rivinius, M. E. Shultz, J. O. Sundqvist, R. H. D. Townsend, A. ud-Doula, J.-C. Bouret, J. Braithwaite, M. Briquet, A. C. Carciofi, A. David-Uraz, C. P. Folsom, A. W. Fullerton, B. Leroy, W. L. F. Marcolino, A. F. J. Moffat, Y. Nazé, N. S. Louis, M. Aurière, S. Bagnulo, J. D. Bailey, R. H. Barbá, A. Blazère, T. Böhm, C. Catala, J.-F. Donati, L. Ferrario, D. Harrington, I. D. Howarth, R. Ignace, L. Kaper, T. Lüftinger, R. Prinja, J. S. Vink, W. W. Weiss, I. Yakunin, The MiMeS survey of magnetism in massive stars: Introduction and overview. *Mon. Not. R. Astron. Soc.* **456**, 2–22 (2016). [doi:10.1093/mnras/stv2568](https://doi.org/10.1093/mnras/stv2568)
11. J. H. Grunhut, G. A. Wade, C. Neiner, M. E. Oksala, V. Petit, E. Alecian, D. A. Bohlender, J.-C. Bouret, H. F. Henrichs, G. A. J. Hussain, O. Kochukhov, The MiMeS survey of Magnetism in Massive Stars: Magnetic analysis of the O-type stars. *Mon. Not. R. Astron. Soc.* **465**, 2432–2470 (2017). [doi:10.1093/mnras/stw2743](https://doi.org/10.1093/mnras/stw2743)
12. A. de la Chevrotière, N. St-Louis, A. F. J. Moffat, MiMeS Collaboration. *Astrophys. J.* **781**, 73 (2014).

13. M. Dorsch, N. Reindl, I. Pelisoli, U. Heber, S. Geier, A. G. Istrate, S. Justham, Discovery of a highly magnetic He-sdO star from a double-degenerate binary merger. *Astron. Astrophys.* **658**, L9 (2022). [doi:10.1051/0004-6361/202142880](https://doi.org/10.1051/0004-6361/202142880)
14. I. Pelisoli, M. Dorsch, U. Heber, B. Gänsicke, S. Geier, T. Kupfer, P. Németh, S. Scaringi, V. Schaffenroth, Discovery and analysis of three magnetic hot subdwarf stars: Evidence for merger-induced magnetic fields. *Mon. Not. R. Astron. Soc.* **515**, 2496–2510 (2022). [doi:10.1093/mnras/stac1069](https://doi.org/10.1093/mnras/stac1069)
15. M. E. Shultz, O. Kochukhov, J. Labadie-Bartz, A. David-Uraz, S. P. Owocki, Detection of an extremely strong magnetic field in the double-degenerate binary merger product HD 144941. *Mon. Not. R. Astron. Soc.* **507**, 1283–1295 (2021). [doi:10.1093/mnras/stab2162](https://doi.org/10.1093/mnras/stab2162)
16. J. E. Steiner, A. S. Oliveira, The qWR star HD 45166. *Astron. Astrophys.* **444**, 895–904 (2005). [doi:10.1051/0004-6361:20052782](https://doi.org/10.1051/0004-6361:20052782)
17. W. R. Hamann, G. Gräfener, A. Liermann, R. Hainich, A. A. C. Sander, T. Shenar, V. Ramachandran, H. Todt, L. M. Oskinova, The Galactic WN stars revisited. *Astron. Astrophys.* **625**, A57 (2019). [doi:10.1051/0004-6361/201834850](https://doi.org/10.1051/0004-6361/201834850)
18. Y. Götberg, S. E. de Mink, J. H. Groh, T. Kupfer, P. A. Crowther, E. Zapartas, M. Renzo, Spectral models for binary products: Unifying subdwarfs and Wolf-Rayet stars as a sequence of stripped-envelope stars. *Astron. Astrophys.* **615**, A78 (2018). [doi:10.1051/0004-6361/201732274](https://doi.org/10.1051/0004-6361/201732274)
19. J. H. Groh, A. S. Oliveira, J. E. Steiner, The qWR star HD 45166. *Astron. Astrophys.* **485**, 245–256 (2008). [doi:10.1051/0004-6361:200809511](https://doi.org/10.1051/0004-6361:200809511)
20. J. S. Vink, Winds from stripped low-mass helium stars and Wolf-Rayet stars. *Astron. Astrophys.* **607**, L8 (2017). [doi:10.1051/0004-6361/201731902](https://doi.org/10.1051/0004-6361/201731902)
21. A. A. C. Sander, J. S. Vink, On the nature of massive helium star winds and Wolf-Rayet-type mass-loss. *Mon. Not. R. Astron. Soc.* **499**, 873–892 (2020). [doi:10.1093/mnras/staa2712](https://doi.org/10.1093/mnras/staa2712)
22. T. Shenar, A. Gilkis, J. S. Vink, H. Sana, A. A. C. Sander, Why binary interaction does not necessarily dominate the formation of Wolf-Rayet stars at low metallicity. *Astron. Astrophys.* **634**, A79 (2020). [doi:10.1051/0004-6361/201936948](https://doi.org/10.1051/0004-6361/201936948)
23. N. R. Walborn, Spectral classification of OB stars in both hemispheres and the absolute magnitude calibration. *Astron. J.* **77**, 312 (1972). [doi:10.1086/111285](https://doi.org/10.1086/111285)
24. Y. Nazé, A. ud-Doula, M. Spano, G. Rauw, M. De Becker, N. R. Walborn, New findings on the prototypical Of?p stars. *Astron. Astrophys.* **520**, A59 (2010). [doi:10.1051/0004-6361/201014333](https://doi.org/10.1051/0004-6361/201014333)
25. Materials and methods are available as supplementary materials.
26. V. Petit, S. P. Owocki, G. A. Wade, D. H. Cohen, J. O. Sundqvist, M. Gagne, J. M. Apellaniz, M. E. Oksala, D. A. Bohlender, T. Rivinius, H. F. Henrichs, E. Alecian, R. H. D. Townsend, A. ud-Doula, M. Collaboration, A magnetic confinement versus rotation classification of massive-star magnetospheres. *Mon. Not. R. Astron. Soc.* **429**, 398–422 (2013). [doi:10.1093/mnras/sts344](https://doi.org/10.1093/mnras/sts344)

27. W. R. Hamann, G. Gräfener, A temperature correction method for expanding atmospheres. *Astron. Astrophys.* **410**, 993–1000 (2003). [doi:10.1051/0004-6361/20031308](https://doi.org/10.1051/0004-6361/20031308)
28. A. Sander, T. Shenar, R. Hainich, A. Gímenez-García, H. Todt, W.-R. Hamann, On the consistent treatment of the quasi-hydrostatic layers in hot star atmospheres. *Astron. Astrophys.* **577**, A13 (2015). [doi:10.1051/0004-6361/201425356](https://doi.org/10.1051/0004-6361/201425356)
29. F. R. N. Schneider, N. Langer, A. de Koter, I. Brott, R. G. Izzard, H. H. B. Lau, Bonnsai: A Bayesian tool for comparing stars with stellar evolution models. *Astron. Astrophys.* **570**, A66 (2014). [doi:10.1051/0004-6361/201424286](https://doi.org/10.1051/0004-6361/201424286)
30. J. F. Donati, I. D. Howarth, M. M. Jardine, P. Petit, C. Catala, J. D. Landstreet, J.-C. Bouret, E. Alecian, J. R. Barnes, T. Forveille, F. Paletou, N. Manset, The surprising magnetic topology of Sco: Fossil remnant or dynamo output? *Mon. Not. R. Astron. Soc.* **370**, 629–644 (2006). [doi:10.1111/j.1365-2966.2006.10558.x](https://doi.org/10.1111/j.1365-2966.2006.10558.x)
31. G. A. Wade, I. D. Howarth, R. H. D. Townsend, J. H. Grunhut, M. Shultz, J.-C. Bouret, A. Fullerton, W. Marcolino, F. Martins, Y. Nazé, A. ud Doula, N. R. Walborn, J.-F. Donati, Confirmation of the magnetic oblique rotator model for the Of?p star HD 191612★. *Mon. Not. R. Astron. Soc.* **416**, 3160–3169 (2011). [doi:10.1111/j.1365-2966.2011.19265.x](https://doi.org/10.1111/j.1365-2966.2011.19265.x)
32. G. Gräfener, J. S. Vink, A. de Koter, N. Langer, The Eddington factor as the key to understand the winds of the most massive stars. *Astron. Astrophys.* **535**, A56 (2011). [doi:10.1051/0004-6361/201116701](https://doi.org/10.1051/0004-6361/201116701)
33. P. T. H. Pang, I. Tews, M. W. Coughlin, M. Bulla, C. Van Den Broeck, T. Dietrich, Nuclear Physics Multimessenger Astrophysics Constraints on the Neutron Star Equation of State: Adding NICER’s PSR J0740+6620 Measurement. *Astrophys. J.* **922**, 14 (2021). [doi:10.3847/1538-4357/ac19ab](https://doi.org/10.3847/1538-4357/ac19ab)
34. R. C. Duncan, C. Thompson, Formation of very strongly magnetized neutron stars - Implications for gamma-ray bursts. *Astrophys. J.* **392**, L9 (1992). [doi:10.1086/186413](https://doi.org/10.1086/186413)
35. N. Langer, Standard models of Wolf-Rayet stars. *Astron. Astrophys.* **210**, 93–113 (1989).
36. S. E. Woosley, Bright Supernovae from Magnetar Birth. *Astrophys. J. Lett.* **719**, L204–L207 (2010). [doi:10.1088/2041-8205/719/2/L204](https://doi.org/10.1088/2041-8205/719/2/L204)
37. P. K. Blanchard, E. Berger, M. Nicholl, V. A. Villar, The Pre-explosion Mass Distribution of Hydrogen-poor Superluminous Supernova Progenitors and New Evidence for a Mass–Spin Correlation. *Astrophys. J.* **897**, 114 (2020). [doi:10.3847/1538-4357/ab9638](https://doi.org/10.3847/1538-4357/ab9638)
38. A. Maeder, G. Meynet, Stellar evolution with rotation. VI. The Eddington and Omega - limits, the rotational mass loss for OB and LBV stars. *Astron. Astrophys.* **361**, 159–166 (2000).
39. I. Brott, S. E. de Mink, M. Cantiello, N. Langer, A. de Koter, C. J. Evans, I. Hunter, C. Trundle, J. S. Vink, Rotating massive main-sequence stars. *Astron. Astrophys.* **530**, A115 (2011). [doi:10.1051/0004-6361/201016113](https://doi.org/10.1051/0004-6361/201016113)
40. L. Ferrario, J. E. Pringle, C. A. Tout, D. T. Wickramasinghe, The origin of magnetism on the upper main sequence. *Mon. Not. R. Astron. Soc.* **400**, L71–L74 (2009). [doi:10.1111/j.1745-3933.2009.00765.x](https://doi.org/10.1111/j.1745-3933.2009.00765.x)

41. D. T. Wickramasinghe, C. A. Tout, L. Ferrario, The most magnetic stars. *Mon. Not. R. Astron. Soc.* **437**, 675–681 (2014). [doi:10.1093/mnras/stt1910](https://doi.org/10.1093/mnras/stt1910)
42. F. R. N. Schneider, S. T. Ohlmann, P. Podsiadlowski, F. K. Röpke, S. A. Balbus, R. Pakmor, V. Springel, Stellar mergers as the origin of magnetic massive stars. *Nature* **574**, 211–214 (2019). [doi:10.1038/s41586-019-1621-5](https://doi.org/10.1038/s41586-019-1621-5) [Medline](#)
43. S. Bagnulo, J. D. Landstreet, Multiple Channels for the Onset of Magnetism in Isolated White Dwarfs. *Astrophys. J. Lett.* **935**, L12 (2022). [doi:10.3847/2041-8213/ac84d3](https://doi.org/10.3847/2041-8213/ac84d3)
44. R. F. Webbink, Double white dwarfs as progenitors of R Coronae Borealis stars and Type I supernovae. *Astrophys. J.* **277**, 355 (1984). [doi:10.1086/161701](https://doi.org/10.1086/161701)
45. J. Schwab, E. Quataert, D. Kasen, The evolution and fate of super-Chandrasekhar mass white dwarf merger remnants. *Mon. Not. R. Astron. Soc.* **463**, 3461–3475 (2016). [doi:10.1093/mnras/stw2249](https://doi.org/10.1093/mnras/stw2249)
46. B. Paxton, L. Bildsten, A. Dotter, F. Herwig, P. Lesaffre, F. Timmes, Modules for Experiments in Stellar Astrophysics (MESA). *Astrophys. J. Suppl. Ser.* **192** (Supp.), 3 (2011). [doi:10.1088/0067-0049/192/1/3](https://doi.org/10.1088/0067-0049/192/1/3)
47. P. Harmanec, Stellar masses and radii based on modern binary data. *Bull. Astron. Inst. Czechoslov.* **39**, 329–345 (1988).
48. T. Shenar, L. M. Oskinova, S. P. Järvinen, P. Luckas, R. Hainich, H. Todt, S. Hubrig, A. A. C. Sander, I. Ilyin, W.-R. Hamann, A combined HST and XMM-Newton campaign for the magnetic O9.7 V star HD 54879. *Astron. Astrophys.* **606**, A91 (2017). [doi:10.1051/0004-6361/201731291](https://doi.org/10.1051/0004-6361/201731291)
49. S. Toonen, S. Portegies Zwart, A. S. Hamers, D. Bandopadhyay, The evolution of stellar triples. *Astron. Astrophys.* **640**, A16 (2020). [doi:10.1051/0004-6361/201936835](https://doi.org/10.1051/0004-6361/201936835)
50. D. R. Gies, K. Shepard, P. Wysocki, R. Klement, The Transformative Journey of HD 93521. *Astron. J.* **163**, 100 (2022). [doi:10.3847/1538-3881/ac43be](https://doi.org/10.3847/1538-3881/ac43be)
51. T. Shenar, A massive helium star with a sufficiently strong magnetic field to form a magnetar, version 2, Zenodo (2023); <https://doi.org/10.5281/zenodo.8040752>.
52. powr-code/PoWR: v20220809, Zenodo (2022); <https://doi.org/10.5281/zenodo.7217731>.
53. J. F. Donati, C. Catala, J. D. Landstreet, P. Petit, “Solar Polarization 4: proceedings of a meeting held in Boulder, Colorado, USA, 19-23 September 2005”, vol. 358 of *Astronomical Society of the Pacific Conference Series*, R. Casini, B. W. Lites, Eds. (2006), p. 362.
54. E. Martioli, D. Teeple, N. Manset, “CFHT data processing and calibration ESPaDOnS pipeline: Upena and OPERA (optical spectropolarimetry)”, in *Proceedings of the conference Telescopes from Afar*, S. Gajadhar *et al.*, Eds. (2011), p. 63.
55. Espectrógrafo Coudé, Laboratório Nacional de Astrofísica, https://www.gov.br/lna/pt-br/composicao-1/coast/obs/opd/instrumentacao/manual/manual_160mopd_cap3.pdf
56. A. Kaufer *et al.*, Commissioning FEROS, the new high-resolution spectrograph at La-Silla. *Messenger* **95**, 8–12 (1999).

57. G. Raskin, H. Van Winckel, H. Hensberge, A. Jorissen, H. Lehmann, C. Waelkens, G. Avila, J.-P. De Cuyper, P. Degroote, R. Dubosson, L. Dumortier, Y. Frémat, U. Laux, B. Michaud, J. Morren, J. Perez Padilla, W. Pessemier, S. Prins, K. Smolders, S. Van Eck, J. Winkler, HERMES: A high-resolution fibre-fed spectrograph for the Mercator telescope. *Astron. Astrophys.* **526**, A69 (2011). [doi:10.1051/0004-6361/201015435](https://doi.org/10.1051/0004-6361/201015435)
58. A. J. Willis, D. J. Stickland, The enigmatic composite system HD 45166 - B8 V + qWR or SdO? *Mon. Not. R. Astron. Soc.* **203**, 619–635 (1983). [doi:10.1093/mnras/203.3.619](https://doi.org/10.1093/mnras/203.3.619)
59. A. J. Willis, I. D. Howarth, D. J. Stickland, S. R. Heap, The ultraviolet variability of HD 45166 (qWR + B8 V) - Evidence for stellar wind radiative instabilities. *Astrophys. J.* **347**, 413 (1989). [doi:10.1086/168129](https://doi.org/10.1086/168129)
60. A. J. Willis, A. W. Burnley, “Astrophysics in the Far Ultraviolet: Five Years of Discovery with FUSE”, vol. 348 of *Astronomical Society of the Pacific Conference Series*, G. Sonneborn, H. W. Moos, B. G. Andersson, eds. (2006), p. 139.
61. K. N. Abazajian, J. K. Adelman-McCarthy, M. A. Agüeros, S. S. Allam, C. A. Prieto, D. An, K. S. J. Anderson, S. F. Anderson, J. Annis, N. A. Bahcall, C. A. L. Bailer-Jones, J. C. Barentine, B. A. Bassett, A. C. Becker, T. C. Beers, E. F. Bell, V. Belokurov, A. A. Berlind, E. F. Berman, M. Bernardi, S. J. Bickerton, D. Bizyaev, J. P. Blakeslee, M. R. Blanton, J. J. Bochanski, W. N. Boroski, H. J. Brewington, J. Brinchmann, J. Brinkmann, R. J. Brunner, T. Budavári, L. N. Carey, S. Carliles, M. A. Carr, F. J. Castander, D. Cinabro, A. J. Connolly, I. Csabai, C. E. Cunha, P. C. Czarapata, J. R. A. Davenport, E. de Haas, B. Dilday, M. Doi, D. J. Eisenstein, M. L. Evans, N. W. Evans, X. Fan, S. D. Friedman, J. A. Frieman, M. Fukugita, B. T. Gänsicke, E. Gates, B. Gillespie, G. Gilmore, B. Gonzalez, C. F. Gonzalez, E. K. Grebel, J. E. Gunn, Z. Györy, P. B. Hall, P. Harding, F. H. Harris, M. Harvanek, S. L. Hawley, J. J. E. Hayes, T. M. Heckman, J. S. Hendry, G. S. Hennessy, R. B. Hindsley, J. Hoblitt, C. J. Hogan, D. W. Hogg, J. A. Holtzman, J. B. Hyde, S. Ichikawa, T. Ichikawa, M. Im, Ž. Ivezić, S. Jester, L. Jiang, J. A. Johnson, A. M. Jorgensen, M. Jurić, S. M. Kent, R. Kessler, S. J. Kleinman, G. R. Knapp, K. Konishi, R. G. Kron, J. Krzesinski, N. Kuropatkin, H. Lampeitl, S. Lebedeva, M. G. Lee, Y. S. Lee, R. F. Leger, S. Lépine, N. Li, M. Lima, H. Lin, D. C. Long, C. P. Loomis, J. Loveday, R. H. Lupton, E. Magnier, O. Malanushenko, V. Malanushenko, R. Mandelbaum, B. Margon, J. P. Marriner, D. Martínez-Delgado, T. Matsubara, P. M. McGehee, T. A. McKay, A. Meiksin, H. L. Morrison, F. Mullally, J. A. Munn, T. Murphy, T. Nash, A. Nebot, E. H. Neilsen, H. J. Newberg, P. R. Newman, R. C. Nichol, T. Nicinski, M. Nieto-Santisteban, A. Nitta, S. Okamura, D. J. Oravetz, J. P. Ostriker, R. Owen, N. Padmanabhan, K. Pan, C. Park, G. Pauls, J. Peoples, W. J. Percival, J. R. Pier, A. C. Pope, D. Pourbaix, P. A. Price, N. Purger, T. Quinn, M. J. Raddick, P. R. Fiorentin, G. T. Richards, M. W. Richmond, A. G. Riess, H.-W. Rix, C. M. Rockosi, M. Sako, D. J. Schlegel, D. P. Schneider, R.-D. Scholz, M. R. Schreiber, A. D. Schwope, U. Seljak, B. Sesar, E. Sheldon, K. Shimasaku, V. C. Sibley, A. E. Simmons, T. Sivarani, J. A. Smith, M. C. Smith, V. Smolčić, S. A. Snedden, A. Stebbins, M. Steinmetz, C. Stoughton, M. A. Strauss, M. SubbaRao, Y. Suto, A. S. Szalay, I. Szapudi, P. Szkody, M. Tanaka, M. Tegmark, L. F. A. Teodoro, A. R. Thakar, C. A. Tremonti, D. L. Tucker, A. Uomoto, D. E. Vanden Berk, J. Vandenberg, S. Vidrih, M. S. Vogeley, W. Voges, N. P. Vogt, Y. Wadadekar, S. Watters, D. H. Weinberg, A. A. West, S. D. M. White, B. C. Wilhite, A. C. Wonders, B. Yanny, D. R. Yocum, D. G. York, I. Zehavi, S. Zibetti, D. B. Zucker,

- The Seventh Data Release of the Sloan Digital Sky Survey. *Astrophys. J. Suppl. Ser.* **182** (suppl.), 543–558 (2009). [doi:10.1088/0067-0049/182/2/543](https://doi.org/10.1088/0067-0049/182/2/543)
62. N. Zacharias *et al.*, “The Naval Observatory Merged Astrometric Dataset (NOMAD)”, American Astronomical Society Meeting 205, vol. 205 of *Bulletin of the American Astronomical Society*, p. 1418 (2004).
63. A. Z. Bonanos, D. L. Massa, M. Sewilo, D. J. Lennon, N. Panagia, L. J. Smith, M. Meixner, B. L. Babler, S. Bracker, M. R. Meade, K. D. Gordon, J. L. Hora, R. Indebetouw, B. A. Whitney, *Spitzer* Sage Infrared Photometry of Massive Stars in the Large Magellanic Cloud. *Astron. J.* **138**, 1003–1021 (2009). [doi:10.1088/0004-6256/138/4/1003](https://doi.org/10.1088/0004-6256/138/4/1003)
64. E. L. Wright, P. R. M. Eisenhardt, A. K. Mainzer, M. E. Ressler, R. M. Cutri, T. Jarrett, J. D. Kirkpatrick, D. Padgett, R. S. McMillan, M. Skrutskie, S. A. Stanford, M. Cohen, R. G. Walker, J. C. Mather, D. Leisawitz, T. N. Gautier, I. McLean, D. Benford, C. J. Lonsdale, A. Blain, B. Mendez, W. R. Irace, V. Duval, F. Liu, D. Royer, I. Heinrichsen, J. Howard, M. Shannon, M. Kendall, A. L. Walsh, M. Larsen, J. G. Cardon, S. Schick, M. Schwalm, M. Abid, B. Fabinsky, L. Naes, C.-W. Tsai, The Wide-Field Infrared Survey Explorer (Wise): Mission Description and Initial On-Orbit Performance. *Astron. J.* **140**, 1868–1881 (2010). [doi:10.1088/0004-6256/140/6/1868](https://doi.org/10.1088/0004-6256/140/6/1868)
65. G. A. Wade, J. M. Apellániz, F. Martins, V. Petit, J. Grunhut, N. R. Walborn, R. H. Barbá, M. Gagné, E. García-Melendo, J. Jose, A. F. J. Moffat, Y. Nazé, C. Neiner, A. Pellerin, M. P. Ordaz, M. Shultz, S. Simón-Díaz, A. Sota, NGC 1624-2: A slowly rotating, X-ray luminous Of?p star with an extraordinarily strong magnetic field. *Mon. Not. R. Astron. Soc.* **425**, 1278–1293 (2012). [doi:10.1111/j.1365-2966.2012.21523.x](https://doi.org/10.1111/j.1365-2966.2012.21523.x)
66. G. A. Wade, J. F. Donati, J. D. Landstreet, S. L. S. Shorlin, High-precision magnetic field measurements of Ap and Bp stars. *Mon. Not. R. Astron. Soc.* **313**, 851–867 (2000). [doi:10.1046/j.1365-8711.2000.03271.x](https://doi.org/10.1046/j.1365-8711.2000.03271.x)
67. O. Kochukhov, V. Makaganiuk, N. Piskunov, Least-squares deconvolution of the stellar intensity and polarization spectra. *Astron. Astrophys.* **524**, A5 (2010). [doi:10.1051/0004-6361/201015429](https://doi.org/10.1051/0004-6361/201015429)
68. O. Kochukhov, Code for iLSD, <https://www.astro.uu.se/~oleg/soft.html>.
69. V. Petit, D. H. Cohen, G. A. Wade, Y. Nazé, S. P. Owocki, J. O. Sundqvist, A. ud-Doula, A. Fullerton, M. Leutenegger, M. Gagné, X-ray emission from the giant magnetosphere of the magnetic O-type star NGC 1624-2. *Mon. Not. R. Astron. Soc.* **453**, 3288–3299 (2015). [doi:10.1093/mnras/stv1741](https://doi.org/10.1093/mnras/stv1741)
70. A. David-Uraz, C. Erba, V. Petit, A. W. Fullerton, F. Martins, N. R. Walborn, R. MacInnis, R. H. Barbá, D. H. Cohen, J. Maíz Apellániz, Y. Nazé, S. P. Owocki, J. O. Sundqvist, A. ud-Doula, G. A. Wade, Extreme resonance line profile variations in the ultraviolet spectra of NGC 1624-2: Probing the giant magnetosphere of the most strongly magnetized known O-type star. *Mon. Not. R. Astron. Soc.* **483**, 2814–2824 (2019). [doi:10.1093/mnras/sty3227](https://doi.org/10.1093/mnras/sty3227)
71. J. D. Landstreet, The magnetic field and abundance distribution geometry of the peculiar A star 53 Camelopardalis. *Astrophys. J.* **326**, 967 (1988). [doi:10.1086/166155](https://doi.org/10.1086/166155)

72. G. A. Wade, S. Bagnulo, O. Kochukhov, J. D. Landstreet, N. Piskunov, M. J. Stift, LTE spectrum synthesis in magnetic stellar atmospheres. *Astron. Astrophys.* **374**, 265–279 (2001). [doi:10.1051/0004-6361:20010735](https://doi.org/10.1051/0004-6361:20010735)
73. G. Gräfener, L. Koesterke, W. R. Hamann, Line-blanketed model atmospheres for WR stars. *Astron. Astrophys.* **387**, 244–257 (2002). [doi:10.1051/0004-6361:20020269](https://doi.org/10.1051/0004-6361:20020269)
74. J. I. Castor, D. C. Abbott, R. I. Klein, Radiation-driven winds in Of stars. *Astrophys. J.* **195**, 157 (1975). [doi:10.1086/153315](https://doi.org/10.1086/153315)
75. T. Shenar, L. Oskinova, W.-R. Hamann, M. F. Corcoran, A. F. J. Moffat, H. Pablo, N. D. Richardson, W. L. Waldron, D. P. Huenemoerder, J. Maíz Apellániz, J. S. Nichols, H. Todt, Y. Nazé, J. L. Hoffman, A. M. T. Pollock, I. Negueruela, A Coordinated X-Ray and Optical Campaign of the Nearest Massive Eclipsing Binary, Δ Orionis Aa. Iv. A Multiwavelength, Non-Lte Spectroscopic Analysis. *Astrophys. J.* **809**, 135 (2015). [doi:10.1088/0004-637X/809/2/135](https://doi.org/10.1088/0004-637X/809/2/135)
76. M. Asplund, N. Grevesse, A. J. Sauval, P. Scott, The Chemical Composition of the Sun. *Annu. Rev. Astron. Astrophys.* **47**, 481–522 (2009). [doi:10.1146/annurev.astro.46.060407.145222](https://doi.org/10.1146/annurev.astro.46.060407.145222)
77. D. F. Gray, *The Observation and Analysis of Stellar Photospheres*, vol. 20 (Cambridge Univ. Press, 1992).
78. S. Simón-Díaz, Fourier method of determining the rotational velocities in OB stars. *Astron. Astrophys.* **468**, 1063 (2007). [doi:10.1051/0004-6361:20066060](https://doi.org/10.1051/0004-6361:20066060)
79. S. Simón-Díaz, The IACOB project. *Astron. Astrophys.* **562**, A135 (2014). [doi:10.1051/0004-6361/201322758](https://doi.org/10.1051/0004-6361/201322758)
80. iacob-broad, Instituto de Astrofísica de Canarias, <http://research.iac.es/proyecto/iacob/pages/en/useful-tools.php>
81. H. A. Abt, H. Levato, M. Grosso, Rotational Velocities of B Stars. *Astrophys. J.* **573**, 359–365 (2002). [doi:10.1086/340590](https://doi.org/10.1086/340590)
82. E. J. Weber, L. J. Davis, The angular momentum of solar wind. *Astrophys. J.* **148**, 217 (1967). [doi:10.1086/149138](https://doi.org/10.1086/149138)
83. A. ud-Doula, S. P. Owocki, R. H. D. Townsend, Dynamical simulations of magnetically channelled line-driven stellar winds - III. Angular momentum loss and rotational spin-down. *Mon. Not. R. Astron. Soc.* **392**, 1022–1033 (2009). [doi:10.1111/j.1365-2966.2008.14134.x](https://doi.org/10.1111/j.1365-2966.2008.14134.x)
84. J. A. Cardelli, G. C. Clayton, J. S. Mathis, The relationship between infrared, optical, and ultraviolet extinction. *Astrophys. J.* **345**, 245 (1989). [doi:10.1086/167900](https://doi.org/10.1086/167900)
85. Bonnsai, <https://www.astro.uni-bonn.de/stars/bonnsai>
86. Astrocut, <https://astrocut.readthedocs.io/en/latest>
87. D. M. Bowman, M. Michielsen, Towards a systematic treatment of observational uncertainties in forward asteroseismic modelling of gravity-mode pulsators. *Astron. Astrophys.* **656**, A158 (2021). [doi:10.1051/0004-6361/202141726](https://doi.org/10.1051/0004-6361/202141726)

88. D. M. Bowman, Asteroseismology of High-Mass Stars: New Insights of Stellar Interiors With Space Telescopes. *Front. Astron. Space Sci.* **7**, 578584 (2020).
[doi:10.3389/fspas.2020.578584](https://doi.org/10.3389/fspas.2020.578584)
89. S. Zucker, T. Mazeh, Study of spectroscopic binaries with TODCOR. 1: A new two-dimensional correlation algorithm to derive the radial velocities of the two components. *Astrophys. J.* **420**, 806 (1994). [doi:10.1086/173605](https://doi.org/10.1086/173605)
90. T. Shenar, J. Bodensteiner, M. Abdul-Masih, M. Fabry, L. Mahy, P. Marchant, G. Banyard, D. M. Bowman, K. Dsilva, C. Hawcroft, M. Reggiani, H. Sana, The “hidden” companion in LB-1 unveiled by spectral disentangling. *Astron. Astrophys.* **639**, L6 (2020).
[doi:10.1051/0004-6361/202038275](https://doi.org/10.1051/0004-6361/202038275)
91. C. Aerts, J. Puls, M. Godart, M. A. Dupret, Collective pulsational velocity broadening due to gravity modes as a physical explanation for macroturbulence in hot massive stars. *Astron. Astrophys.* **508**, 409–419 (2009). [doi:10.1051/0004-6361/200810471](https://doi.org/10.1051/0004-6361/200810471)
92. M. Newville, T. Stensitzki, D. B. Allen, A. Ingargiola, Non-Linear Least-Squares Minimization and Curve-Fitting for Python, version 0.8.0, Zenodo (2014);
<https://doi.org/10.5281/zenodo.11813>
93. T. Shenar, D. P. Sablowski, R. Hainich, H. Todt, A. F. J. Moffat, L. M. Oskinova, V. Ramachandran, H. Sana, A. A. C. Sander, O. Schnurr, N. St-Louis, D. Vanbeveren, Y. Götberg, W.-R. Hamann, The Wolf–Rayet binaries of the nitrogen sequence in the Large Magellanic Cloud. *Astron. Astrophys.* **627**, A151 (2019). [doi:10.1051/0004-6361/201935684](https://doi.org/10.1051/0004-6361/201935684)
94. G. Rauw *et al.*, A new orbital solution for the massive binary system HD 93403. *Astron. Astrophys.* **360**, 1003–1010 (2000).
95. D. R. Gies, W. G. Bagnuolo Jr., E. C. Ferrara, A. B. Kaye, M. L. Thaller, L. R. Penny, G. J. Peters, *Hubble Space Telescope* Goddard High Resolution Spectrograph Observations of the Be + sdO Binary ϕ Persei. *Astrophys. J.* **493**, 440–450 (1998). [doi:10.1086/305113](https://doi.org/10.1086/305113)
96. J. Bodensteiner, T. Shenar, L. Mahy, M. Fabry, P. Marchant, M. Abdul-Masih, G. Banyard, D. M. Bowman, K. Dsilva, A. J. Frost, C. Hawcroft, M. Reggiani, H. Sana, Is HR 6819 a triple system containing a black hole? *Astron. Astrophys.* **641**, A43 (2020).
[doi:10.1051/0004-6361/202038682](https://doi.org/10.1051/0004-6361/202038682)
97. N. Ivanova, S. Justham, X. Chen, O. De Marco, C. L. Fryer, E. Gaburov, H. Ge, E. Glebbeek, Z. Han, X.-D. Li, G. Lu, T. Marsh, P. Podsiadlowski, A. Potter, N. Soker, R. Taam, T. M. Tauris, E. P. J. van den Heuvel, R. F. Webbink, Common envelope evolution: Where we stand and how we can move forward. *Astron. Astrophys. Rev.* **21**, 59 (2013).
[doi:10.1007/s00159-013-0059-2](https://doi.org/10.1007/s00159-013-0059-2)
98. P. P. Eggleton, Approximations to the radii of Roche lobes. *Astrophys. J.* **268**, 368 (1983).
[doi:10.1086/160960](https://doi.org/10.1086/160960)
99. R. Iaconi, O. De Marco, Speaking with one voice: Simulations and observations discuss the common envelope α parameter. *Mon. Not. R. Astron. Soc.* **490**, 2550–2566 (2019).
[doi:10.1093/mnras/stz2756](https://doi.org/10.1093/mnras/stz2756)

100. Z. Keszthelyi, G. Meynet, C. Georgy, G. A. Wade, V. Petit, A. David-Uraz, The effects of surface fossil magnetic fields on massive star evolution: I. Magnetic field evolution, mass-loss quenching, and magnetic braking. *Mon. Not. R. Astron. Soc.* **485**, 5843–5860 (2019). [doi:10.1093/mnras/stz772](https://doi.org/10.1093/mnras/stz772)
101. T. M. Tauris, N. Langer, P. Podsiadlowski, Ultra-stripped supernovae: Progenitors and fate. *Mon. Not. R. Astron. Soc.* **451**, 2123–2144 (2015). [doi:10.1093/mnras/stv990](https://doi.org/10.1093/mnras/stv990)
102. L. Dessart, D. J. Hillier, E. Livne, S.-C. Yoon, S. Woosley, R. Waldman, N. Langer, Core-collapse explosions of Wolf-Rayet stars and the connection to Type IIb/Ib/Ic supernovae. *Mon. Not. R. Astron. Soc.* **414**, 2985–3005 (2011). [doi:10.1111/j.1365-2966.2011.18598.x](https://doi.org/10.1111/j.1365-2966.2011.18598.x)
103. A. Gilkis, I. Arcavi, How much hydrogen is in Type Ib and IIb supernova progenitors? *Mon. Not. R. Astron. Soc.* **511**, 691–712 (2022). [doi:10.1093/mnras/stac088](https://doi.org/10.1093/mnras/stac088)
104. J. E. Steiner, M. P. Diaz, The V Sagittae Stars. *Publ. Astron. Soc. Pac.* **110**, 276–282 (1998). [doi:10.1086/316139](https://doi.org/10.1086/316139)
105. A. S. Oliveira, J. E. Steiner, D. Cieslinski, WR 7a: A V Sagittae or a qWR star? *Mon. Not. R. Astron. Soc.* **346**, 963–967 (2003). [doi:10.1111/j.1365-2966.2003.07157.x](https://doi.org/10.1111/j.1365-2966.2003.07157.x)
106. A. S. Oliveira, J. E. Steiner, M. P. Diaz, The Multiple Spectroscopic and Photometric Periods of DI Crucis (WR 46). *Publ. Astron. Soc. Pac.* **116**, 311–325 (2004). [doi:10.1086/382899](https://doi.org/10.1086/382899)
107. S. Hubrig, M. Schöller, A. Cikota, S. P. Järvinen, The search for magnetic fields in two Wolf-Rayet stars and the discovery of a variable magnetic field in WR 55. *Mon. Not. R. Astron. Soc.* **499**, L116–L120 (2020). [doi:10.1093/mnras/slaa170](https://doi.org/10.1093/mnras/slaa170)
108. H. Todt, M. Peña, W. R. Hamann, G. Gräfener, The central star of the planetary nebula PB 8: A Wolf-Rayet-type wind of an unusual WN/WC chemical composition. *Astron. Astrophys.* **515**, A83 (2010). [doi:10.1051/0004-6361/200912183](https://doi.org/10.1051/0004-6361/200912183)
109. M. Steffen, S. Hubrig, H. Todt, M. Schöller, W.-R. Hamann, C. Sandin, D. Schönberner, Weak magnetic fields in central stars of planetary nebulae? *Astron. Astrophys.* **570**, A88 (2014). [doi:10.1051/0004-6361/201423842](https://doi.org/10.1051/0004-6361/201423842)
110. C. A. L. Bailer-Jones, J. Rybizki, M. Fouesneau, M. Demleitner, R. Andrae, Estimating Distances from Parallaxes. V. Geometric and Photogeometric Distances to 1.47 Billion Stars in Gaia Early Data Release 3. *Astron. J.* **161**, 147 (2021). [doi:10.3847/1538-3881/abd806](https://doi.org/10.3847/1538-3881/abd806)